A Detailed Open-Source Musculoskeletal Model of the Human Lumbar Spine

by

Miguel Christophy

B.S. University of California, Berkeley, 2009

A report submitted in partial satisfaction of the

requirements for the degree of

Masters of Science, Plan II

in

Mechanical Engineering

in the

Graduate Division

of the

University of California, Berkeley

Committee in charge:

Professor Oliver M. O'Reilly, Chair

Professor Tony Keaveny

Spring 2010

The report of Miguel Christophy is approved:

_____

Chair   Date

_____

                                                         Date

University of California at Berkeley

Spring 2010

To my best friend Joseph P. Wood,

Rest In Peace

Table of Contents

List of Figures

Acknowledgments

I would like to express my deepest gratitude and appreciation towards my mentor, Professor Oliver M. O'Reilly for guiding me through my undergraduate and graduate studies, and my research. In addition, I express my gratitude to Professor Jeffrey Lotz for his support and expertise during this project.

I would also like to thank Nur Adila Faruk Senan with her help in working out a lot of the tedious details necessary in building this model, and her guidance through this work. In addition, I acknowledge the OpenSim team, especially Ayman Habib and Edith M. Arnold, for their continued technical support and their gracious sharing of helpful software applications.

Chapter 1

Introduction

The lumbar spine is of continued concern for physicians and patients. It is estimated that up to 85% of all people will report having back pain at some time in their lifetime [5]. In 1998, it was estimated that patients with back pain spend more than $90 billion annually (1% of U.S. GDP) in health care costs [58]. In a 2002 survey, 26% of U.S. adults reported low back pain, and it was estimated that in 2005, about 33.3 million U.S. adults have spine problems [65]. Despite advancements in medical treatment and spending on this issue, the annual per capita health expenditure in U.S. adults has increased by 65% from 1997 to 2005 and people with low back pain have been shown to spend 73% more on health expenses per year [65]. It has generally been considered that the cause of back pain is primarily biomechanical [1, 68, 111]. For this reason, musculoskeletal models are of great interest to researchers in biomechanics, as they provide an inexpensive and efficient method to determine the different parameters of interest such as muscle activation, joint torques and forces, the contributions of passive and active stiffness elements, optimal posture, and the like that can be used to differentiate the motion of subjects with and without lower back

pain. In addition, these models permit the numerical replication and analysis of various biomechanical experiments for a wide variety of subjects in a relatively simple and user-friendly manner. This is especially advantageous for physicians and medical practitioners who have limited time and desire quick results.

The last decade has shown exponential growth in open source software projects [26]. This growth has demonstrated the power of open-source, research based communities, such as Wikipedia, in combining knowledge towards a centralized goal [50]. The SimTK initiative and the OpenSim [23] community is a great example of this application in the biomechanics arena. Users can download the OpenSim software for free and use it to to create their own models, improve upon existing ones, or, alternatively, simply employ any of the available models, to analyze biomechanical data. The benefits are numerous and include the ability to build upon the contribution of others instead of needing to start from scratch, a better understanding of existing models, the potential for comparing kinematical data from different research groups on a common platform as well as the fostering of an environment of cooperation in the biomechanics community. Improvements of existing models as well as newly developed ones can be obtained and analyzed relatively effortlessly. In short, the development of an open-source musculoskeletal model of the lumbar spine can open the door for other researchers' contributions and refinements paving the way for the establishment of a penultimate model that accurately mimics the human lumbar spine in a relatively small amount of time.

Several models of the human lumbar spine have been presented in the literature [14, 20, 22, 28, 52, 71, 95, 96]. However, there have been several limitations and drawbacks to these models. In particular, these models have either been created with local software with

proprietary software that is not easily attainable, or have not been made available to the public. In addition, no model has yet to combine the detailed lumbar musculature with the necessary accurate musculotendon parameters as defined by Zajac [116].

This reports attempts to address this deficit by presenting an open-source, detailed musculoskeletal model of the human lumbar spine. The 8 main muscle groups of the lower back are incorporated via their associated 238 muscle fascicles [14]. Muscle wrapping surfaces and via points have been utilized extensively to ensure physiological lines of action. In addition, new data for the extensive muscle parameters necessary for modeling the 238 actuators (or muscle fascicles) as a Hill-Type Model [43, 116] is presented in Table A.2.

This report is organized as follows. In Chapter 2, we examine the use of rotation tensors for describing motions as well as provide a brief summary on the determination of the instantaneous axes of rotation (IAR) of each joint. We also explain the basic kinematics working behind the OpenSim musculoskeletal program [23, 24], and its Dynamics Engine. We also present a literature review of the extensive kinematic studies of the lumbar spine motion using various techniques: CT, MRI, Dual Video Fluoroscopy, and Kirschner-wires. Chapter 3 goes into further detail about muscle parameters, and their use for determining musculotendon force, and moments. In Chapter 4, we examine the literature with respect to work on the lumbar spine musculature, in particular, focus on the extensive anatomical work conducted by Bogduk and Macintosh in the 1980s [14, 12]. Lastly, in Chapter 5 we present our OpenSim musculoskeletal model of the lumbar spine, describe the assumptions employed, and compare the ensuing results to relevant experimental data.

Chapter 2

Background from Biomechanics

2.1 Rotations

In order to parametrize motions between bodies, we must introduce what is known as a tensor. For the sake of simplicity, we will define a tensor $\mathbf{A}$ as a linear transformation of the Euclidean vector space E into itself. A rotation tensor $\mathbf{R}$ is a subset of the tensor space L and is defined as a proper-orthogonal tensor ($\mathbf{R}\mathbf{R}^T = \mathbf{I}$) which transforms vectors from the fixed frame of reference into the moving frame of reference:

$$\mathbf{e}_i = \mathbf{R}\mathbf{E}_i = R_{ki}\mathbf{E}_k. \tag{2.1}$$

From (2.1), we can write $\mathbf{R}$ as

$$\mathbf{R} = R_{ik}\mathbf{E}_i \otimes \mathbf{E}_k = R_{ik}\mathbf{e}_i \otimes \mathbf{e}_k = \mathbf{e}_i \otimes \mathbf{E}_i, \tag{2.2}$$

Note in the above representation that the tensor $\mathbf{R}$ has nine components R_{ik}. Euler represents a rotation tensor by its axis of rotation $\mathbf{r}$ and an angle of rotation θ by the

following:

$$
\begin{aligned}
\mathbf{R}(\theta, \mathbf{r}) &= \cos(\theta)\mathbf{I} + (1 - \cos(\theta))(\mathbf{r} \otimes \mathbf{r}) - \sin(\theta)(\boldsymbol{\epsilon}\mathbf{r}) \\
&= \cos(\theta)(\mathbf{I} - \mathbf{r} \otimes \mathbf{r}) - \sin(\theta)(\boldsymbol{\epsilon}\mathbf{r}) + \mathbf{r} \otimes \mathbf{r}.
\end{aligned}
\tag{2.3}
$$

Furthermore, commonly used in the dynamics of aircrafts, automotives, and in biomechanics, Euler presents a means of representing motion by three rotations about three different axes. This is known as the Euler angle representation. Essentially, this representation is a combination of three rotation tensors:

$$
\mathbf{R} = \mathbf{R}(\nu^1, \nu^2, \nu^3) = \mathbf{R}(\nu^3, \mathbf{g}_3)\mathbf{R}(\nu^2, \mathbf{g}_2)\mathbf{R}(\nu^1, \mathbf{g}_1),
\tag{2.4}
$$

where $\{\nu^i\}$ are the Euler angles, $\{\mathbf{g}_i\}$ are the set of unit vectors known as the Euler basis and $\mathbf{R}(\nu^i, \mathbf{g}_i)$ is defined by Eq. 2.3. For the purpose of lumbar motion, we will employ the 3-1-2 set of Euler angles:

$$
\begin{bmatrix} \mathbf{g}_1 \\ \mathbf{g}_2 \\ \mathbf{g}_3 \end{bmatrix} = \begin{bmatrix} 0 & 0 & 1 \\ \cos(\psi) & \sin(\psi) & 0 \\ -\cos(\theta)\sin(\psi) & \cos(\theta)\cos(\psi) & \sin(\theta) \end{bmatrix} \begin{bmatrix} \mathbf{E}_1 \\ \mathbf{E}_2 \\ \mathbf{E}_3 \end{bmatrix}
\tag{2.5}
$$

Therefore, the body will undergo a rotation of an angle ψ about $\mathbf{E}_3$, θ about $\mathbf{E}_1$, and γ about $\mathbf{E}_2$, as shown in Fig. 2.4. This set of Euler angles is asymmetric, and is convenient because its only singularity occurs if the second angle, θ, is $\pm\pi/2$. Since lateral bending (rotation about $\mathbf{E}_1$) of each vertebrae is limited to a maximum of about ± 10 degrees [9], there should be no worry about reaching this singularity. Using the Euler angle representation, as in Eq. 2.4, the rotation tensor $\mathbf{R}$ takes the matrix representation with the following

5

components, R_{ik}:

$$
\begin{bmatrix}
R_{11} & R_{12} & R_{13} \\
R_{21} & R_{22} & R_{23} \\
R_{31} & R_{32} & R_{33}
\end{bmatrix}
=
\begin{bmatrix}
\cos(\gamma) & 0 & -\sin(\gamma) \\
0 & 1 & 0 \\
\sin(\gamma) & 0 & \cos(\gamma)
\end{bmatrix}
\begin{bmatrix}
1 & 0 & 0 \\
0 & \cos(\theta) & \sin(\theta) \\
0 & -\sin(\theta) & \cos(\theta)
\end{bmatrix}
\begin{bmatrix}
\cos(\psi) & \sin(\psi) & 0 \\
-\sin(\psi) & \cos(\psi) & 0 \\
0 & 0 & 1
\end{bmatrix}
\tag{2.6}
$$

2.2 Rigid Body Motion

The general motion of a rigid body is characterized with six general coordinate: three rotations, and three tranlsations. This motion is depicted in Fig. 2.1. The transformation brings forth the following result:

$$
\mathbf{x}(t) = \mathbf{Q}(t)\mathbf{X} + \mathbf{d}(t).
\tag{2.7}
$$

Here, $\mathbf{x}(t)$ is the position of an arbitrary material point on the rigid body, $\mathbf{X}$ is the point's initial position, $\mathbf{Q}(t)$ is the rotation tensor, and $\mathbf{d}(t)$ is the displacement of the rigid body. The fixed body has its coordinate system in the fixed Cartesian basis $\{\mathbf{E}_1, \mathbf{E}_2, \mathbf{E}_3\}$, while the moving body, $\mathcal{B}_2$ lies in the corotational basis $\{\mathbf{e}_1, \mathbf{e}_2, \mathbf{e}_3\}$, which transforms according to Eq. 2.7.
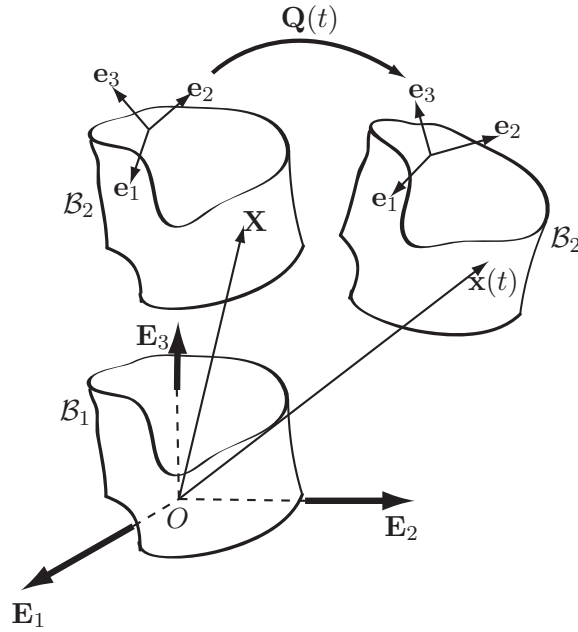
Figure 2.1: *Schematic of two rigid bodies: $\mathcal{B}_1$, fixed, and $\mathcal{B}_2$, moving relative to $\mathcal{B}_1$.*

2.3 Determination of the Helical Axis

The helical axis is a convenient way to represent joint motions, yet it is sometimes difficult to visualize. Fig. 2.2 is a schematic of a rigid body motion through the helical axis. The SimBody toolkit does not employ this technique to represent motion, as Euler Angles yield more stable transformations, less subject to singularities. However, it is important to understand the helical axis, as it has a strong use in biomechanics for it simplicity of representation.

For a rotation tensor $\mathbf{Q}(t)$, its instantaneous axis of rotation, $\mathbf{s}(t)$, is invariant when $\mathbf{Q}(t)$ is operated upon it: $\mathbf{Q}(t)\mathbf{s}(t) = \mathbf{s}(t)$. Therefore, $\mathbf{s}(t)$ is the real eigenvector of $\mathbf{Q}(t)$ and the
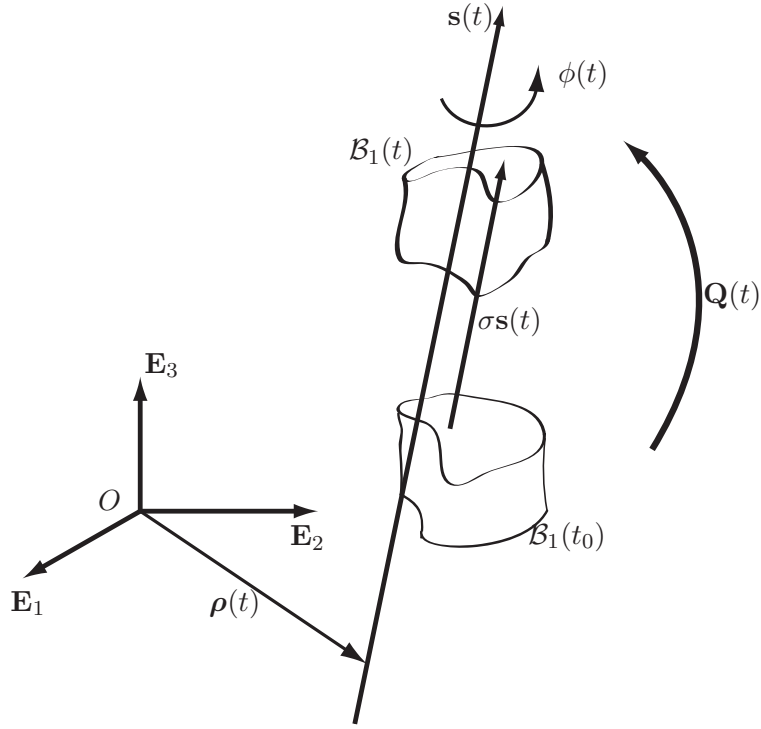
Figure 2.2: *Schematic of the motion of a rigid body, $\mathcal{B}_1$, depicting the helical axis $\mathbf{s}(t)$, the angle of rotation $\phi(t)$, and the translation $\sigma(t)$ along the axis.*

solution to

$$(\mathbf{Q}(t) - \mathbf{I})\,\mathbf{s}(t) = 0. \tag{2.8}$$

The angle of rotation, $\phi(t)$, can be calculated as follows:

$$\cos(\phi(t)) = \frac{1}{2}(tr(\mathbf{Q}(t)) - 1) \tag{2.9}$$

When the angle of rotation is known, the helical axis can be computed:

$$\mathbf{s}(t) = \frac{1}{2\sin\phi(t)} \begin{bmatrix} Q_{32} - Q_{23} \\ Q_{13} - Q_{31} \\ Q_{21} - Q_{12} \end{bmatrix} \tag{2.10}$$

Furthermore, the amount of translation, $\sigma(t)$, along the helical axis $\mathbf{s}(t)$, is:

$$\sigma(t) = \mathbf{s}(t) \cdot \mathbf{d}(t) \tag{2.11}$$

The previous solutions are straightforward. However, the location of the helical axis, $\boldsymbol{\rho}(t)$, is not well defined. In general, the solution to $\boldsymbol{\rho}(t)$ is as follows:

$$(\mathbf{Q}(t) - \mathbf{I})\boldsymbol{\rho}(t) = \sigma(t)\mathbf{s}(t)\mathbf{d}(t) \tag{2.12}$$

However, $(\mathbf{Q}(t) - \mathbf{I})$ is noninvertible, and hence there is no unique solution to $\boldsymbol{\rho}(t)$ in Eq. 2.12. Therefore, $\boldsymbol{\rho}(t)$ can be solved by setting a component arbitrarily. Of common practice is to solve for the intercept of the helical axis with the $\mathbf{E}_1 - \mathbf{E}_2, \mathbf{E}_1 - \mathbf{E}_3$, or $\mathbf{E}_2 - \mathbf{E}_3$ planes, or solve for $\boldsymbol{\rho}(t)$ to be normal to $\mathbf{s}(t)$, $\mathbf{s}(t) \cdot \boldsymbol{\rho}(t) = 0$. The latter solution simplifies to the following equation:

$$\boldsymbol{\rho}(t) = \frac{1}{2}\left(\mathbf{d}(t) - \sigma\mathbf{s}(t) + \cot\left(\frac{\phi(t)}{2}\right)\mathbf{s}(t) \times \mathbf{d}(t)\right) \tag{2.13}$$

2.4   Joints

In dealing with the motion of a rigid body relative to another rigid body, the OpenSim program employs the definition of a joint. The joint defines the axes of rotation and the axes of translation as well as the coordinates which define the motions.

Fig. 2.3 shows how OpenSim defines a child body relative to its parent body, and about which point the transformation occurs. As shown in Fig. 2.1, one can also define the child body by a vector $\mathbf{X}$ in its initial fixed state, and by a vector $\mathbf{x}$ in the corotational basis in its transformed state.
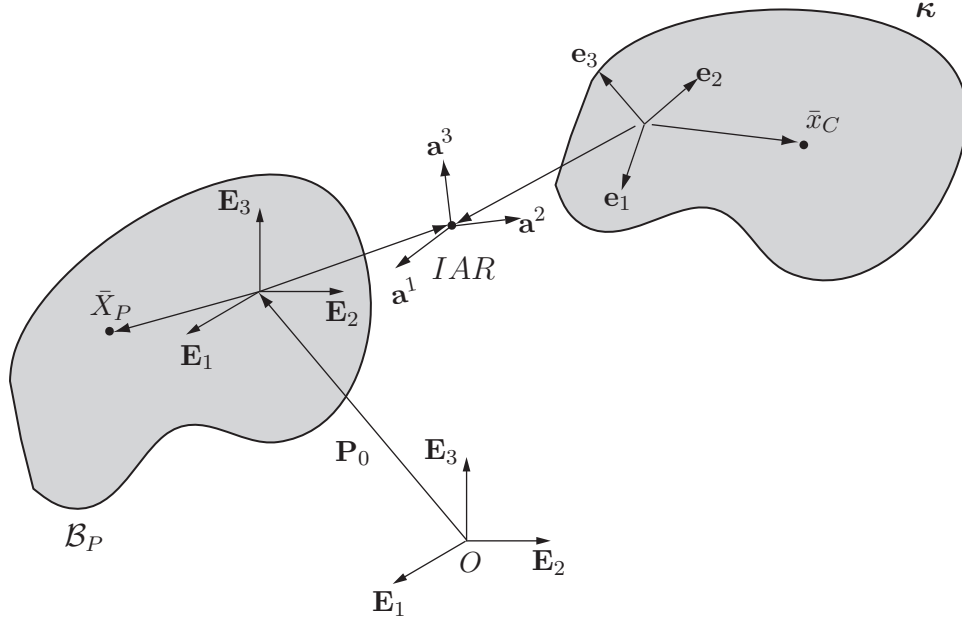
Figure 2.3: *A fixed parent body is located relative to the ground origin O by $\mathbf{P}_0$. The joint, located at the instantaneous axis of rotation, IAR, connects the parent body $\mathcal{B}_P$ and its child body $\boldsymbol{\kappa}$. The child body $\boldsymbol{\kappa}$ is able to spatially transform about the axes of rotation, given by $\{\mathbf{a}^1, \mathbf{a}^2, \mathbf{a}^3\}$. The center of mass and inertia of each body are defined with respect to their body-fixed frames by the vectors $\bar{\mathbf{X}}_P$ and $\bar{\mathbf{x}}_C$, respectively. This figure also displays the corotational basis $\{\mathbf{e}_1, \mathbf{e}_2, \mathbf{e}_3\}$.*

In OpenSim, there is a variety of the types of joints that may be employed (pin, ball, slider, etc.). The most versatile and common joint is known as a CustomJoint. This joint employs the spatial transform:

$$
{}^{P}\mathbf{X}(q)^{B} = \begin{bmatrix} & & x_4 \\ {}^{P}\mathbf{R}^{B}(x_1, x_2, x_3) & & x_5 \\ & & x_6 \end{bmatrix}, \tag{2.14}
$$

where ${}^{P}\mathbf{R}^{B}$ represents the components of the rotation tensor from the parent body to the

10

child body, q_i are the internal coordinates of the joint and x_i are the spatial coordinates for the rotations and the translations along any arbitrary user-defined axes. The relationship between the generalized coordinates q_i and each of the spatial coordinates x_i within a joint are given by:

$$x_i(q) = \begin{Bmatrix} f_1(q_1, q_2, ..., q_m) \\ f_2(q_1, q_2, ..., q_m) \\ \vdots \\ f_6(q_1, q_2, ..., q_m) \end{Bmatrix}. \tag{2.15}$$

OpenSim also handles coupled coordinates (i.e., integrable constraints), although its limitation is to single-variate functions. In order to couple (or constrain) coordinates, the model maker must make use of the CoordinateCouplerConstraint. This feature uses a function to define the dependent coordinate q_{dep} with respect to an independent coordinate q_{ind}:

$$q_{dep} = f(q_{ind}). \tag{2.16}$$

The coupling constraint then eliminates q_{dep} as an editable coordinate from the coordinate window. OpenSim has capabilities for linear functions, piecewise linear functions, multipliers, GCV Splines, and Cubic Splines. However, at present, there is no multi-variate functional capacity, and hence complex coupling patterns must be treated on a case-by-case basis.

2.4.1 Lumbar Spine Kinematics

For the lumbar spine, the motion of a vertebrae is defined relative to the vertebrae below it. This starts with the $\mathcal{L}_5$ relative to a fixed sacrum $\mathcal{S}_1$, the $\mathcal{L}_4$ relative to $\mathcal{L}_5$, and moves on up to $\mathcal{L}_1$. The joint in this case is the intervertebral disc, which is composed of two

basic components: a central nucleus pulposus surrounded by a peripheral anulus fibrosus. In addition, two layers of cartilage cover the top and bottom of the disc and are known as the vertebral endplates. The function of the intervertebral disc is to allow 6 degree of freedom movement between the vertebrae and to transmit load from one rigid body to the other. Fig. 2.4 represents one representation of the axes of rotation between the $\mathcal{L}_4$ and $\mathcal{L}_5$ vertebrae.
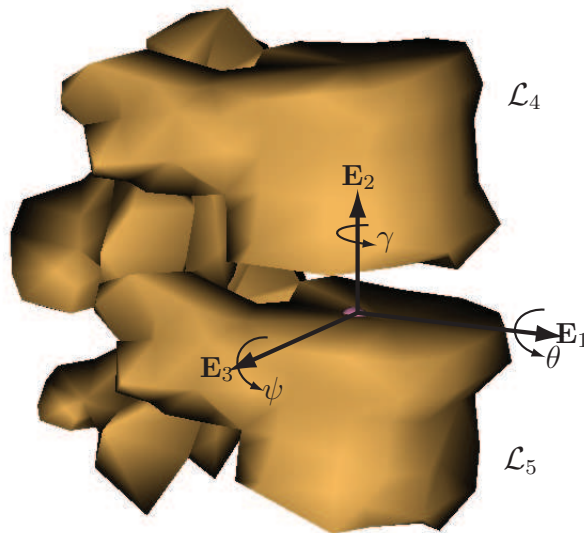
Figure 2.4: *The coordinate system for relative motion at the $\mathcal{L}_4/\mathcal{L}_5$ Joint.*

In order to implement the correct spinal motion within OpenSim, it is convenient to limit the entire system to only 3 coordinates: *flexion-extension* (ψ about $\mathbf{E}_3$), *axial rotation* (θ about $\mathbf{E}_2$), and *lateral bending* (γ about $\mathbf{E}_1$), defined as the angle between the torso and ribcage and the sacrum. In order to simplify the model from a 30 degrees-of-freedom system to a 3 degrees-of-freedom system, we have used a series of kinematic constraint functions such as Eq. 2.16, as explained in Sec. 2.4, in a method similar to Vasavada *et al.* [104]. These constraints define the rotations and translations necessary at each joint level in order to create the overall joint angle (i.e. flexion-extension).

The kinematic coordinate constraints implemented during flexion-extension are plotted in Fig. 2.5. This is a plot of the relative *primary* rotations (about $\mathbf{E}_3$) of the 5 joints during a flexion-extension movement, and excludes any coupling or translational motion. This data was presented by Wong *et al.* [114], and measured in-vivo using dual video fluoroscopy (DVF), a highly accurate kinematic method: with error of less than 0.3 mm in translation and $0.7°$ in rotation [106]. The downside to this study is that Wong *et al.* have not presented any coupling data for this motion, nor do they present the kinematics for any other trunk motion.
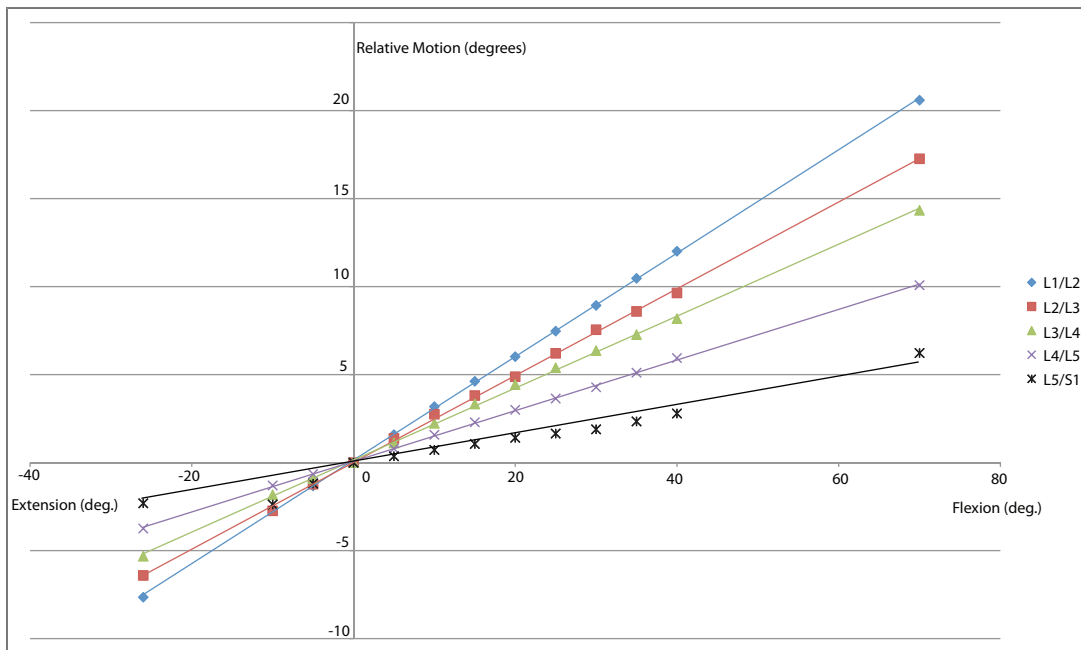
Figure 2.5: *The relative motion of each vertebral level as a function of the overall flexion-extension angle. This data is a linear best fit from Wong et al. [114].*

Characterizing the motion of the joints in this way is not completely physiological, as it does not incorporate the passive structures within the intervertebral disc, which is covered

in the next section.

White and Panjabi's in-depth review of spinal kinematics in 1978 [9] is a valuable primer on the motion of lateral bending. Several studies have investigated these kinematics. Pearcy used an in-vivo 3D X-ray technique in 1984 [85]. In 1989, Yamamoto *et al.* used cadaveric spines in a motion capture system and applied pure moments to determine segmental motion [115]. Since then, several other studies have reported data on ranges of motion during lateral bending [33, 54, 91, 102]. For the kinematic constraints used to describe the primary rotations at each level during lateral bending, data from Rozumalski *et al.* was used [91] as a percentage of the total ROM. Troke *et al.*'s extensive ROM study of 405 asymptomatic subjects presented a total ROM of 29-16 degrees (declining linearly with age) in lateral bending [102]. We chose the data presented for a male 30 years of age, which resulted in a total ROM of $25°$. The data used for lateral bending is shown in Table 2.1:

Table 2.1: *Range of Motion at each vertebral level during maximum lateral bending of* $25°$.

	Lat. Bend. [91]	Axial Rot.	Flex-ext
L1/L2	4.7	0.0[85]	2.0[85]
L2/L3	6.25	2.2[54]	2.1[54]
L3/L4	6.13	3.8[54]	1.3[54]
L4/L5	4.53	2.8[54]	1.9[54]
L5/S1	3.39	1.0[85]	-1.0[85]

Li *et al.* study in 2009, used MR images which were imported into 3D modeling software, presents the most comprehensive coupling data for lateral bending [54]. The pitfall being that only data for the L2/L3, L3/L4, and L4/L5 levels are presented. Data for the other two levels was taken from Pearcy and Tibrewal [85].

14

Studies of axial rotation go as far back as 1967 with Gregersen and Lucas' study using Steinman pins [39]. Lumsden *et al.* studied the kinematics of axial rotation in 1968 using invasive in vivo Steinman pins, yet reported rotation of up to $6°$ at the L5/S1 joint [57]. It is well known that there is a strong coupling nature during axial rotation of the lumbar spine [9, 85]. In particular, axial rotation has been known to cause lateral bending in the opposite direction [79]. In addition, considering that the collagenous fibers of the annulus of the IVD would be irreversibly damaged if stretched beyond 4% of resting length [42], Bogduk calculates that axial rotation of a vertebrae is limited to about $3°$ without injury to the disc [12]. Therefore, any in-vivo data which presents segmental axial rotations greater than $3°$ in a healthy subject is questionable.

Fujii *et al.* performed an extensive in vivo 3D MRI study of the kinematics of axial rotation in 2007 [30]. The accuracy of this system is less than $0.4°$ for rotations, and less than 0.5 mm for translations [47]. Their study rotated the trunk externally in increments of $15°$, up to $45°$, while measuring segmental translations and rotations for all 6 degrees-of-freedom. Their results confirm Panjabi's statement of strong coupling of lateral bending during axial rotation, however the directions are in the opposite of those presented by White *et al.* [9], but agree well with the directions presented by Pearcy *et al.* [85]. Their data presents complex non-linear functions and asymmetric movement patterns. This left-right asymmetric kinematics has been confirmed in a more recent dual fluoroscopic study by Kozanek *et al.* in which he reports 'facet tropism' towards one side [51]. We have simplified the results by Fujii *et al.* by assuming a linear relationship and symmetry in left and right rotation. Lastly, Fujii *et al.* also measured maximum voluntary trunk rotation as $56.1\pm7.5°$. The maximum axial rotation at each level is shown below, extending the linear regression

from $45\,°$ to $56\,°$:

Table 2.2: *Range of Motion at each vertebral level during maximum axial rotation of* $56.1\,°$ *to the left. Negate all values for right AR, except for Flex-ext. which stays positive during the motion. Data from Fujii et al. [30].*

	Axial Rot.	Lat. Bend.	Flex-ext	Lat. Trans.(mm)
L1/L2	1.62	2.12	1.0	0.37
L2/L3	1.87	3.73	1.5	1.50
L3/L4	2.37	4.73	1.6	2.00
L4/L5	2.37	2.49	1.5	1.37
L5/S1	2.20	-0.87	2.6	1.24

2.4.2   Intervertebral Stiffness Matrix

The complex fibrous structure of the intervertebral disc makes it a passive stiffness structure. In order to parametrize its properties, Panjabi proposed the use of a stiffness matrix K in 1976 [82]. Stokes and Garnder-Morse implement this in their lumbar spine model [96], which has lead to several in-vitro experimental studies [31, 71, 80, 98] on the determination of the 36 components:

$$\mathsf{K} = \begin{bmatrix} K_{11} & K_{12} & K_{13} & K_{14} & K_{15} & K_{16} \\ K_{21} & K_{22} & K_{23} & K_{24} & K_{25} & K_{26} \\ K_{31} & K_{32} & K_{33} & K_{34} & K_{35} & K_{36} \\ K_{41} & K_{42} & K_{43} & K_{44} & K_{54} & K_{46} \\ K_{51} & K_{52} & K_{53} & K_{54} & K_{55} & K_{56} \\ K_{61} & K_{62} & K_{63} & K_{64} & K_{65} & K_{66} \end{bmatrix} \tag{2.17}$$

This stiffness matrix is quite convenient in representing the complex coupling in the intervertebral disc, as well as the compliance of the disc. In addition, it is convenient when modeling changes in disc properties: one only has to change the 36 components of K, and the kinematics and passive structure of the joints will change. The relationship of the intervertebral stiffness to the forces and moments applied at the joint follow the simple relationship:

$$F = Kd \tag{2.18}$$

where F is a 6 component vector with 3 force components, and 3 moment components, K is the 6X6 stiffness matrix, and d is a 6 component displacement of the generalized coordinates (3 for translations, and 3 for rotations):

$$\begin{bmatrix} F_x \\ F_y \\ F_z \\ M_x \\ M_y \\ M_z \end{bmatrix} = \begin{bmatrix} K_{11} & K_{12} & \cdots & K_{16} \\ K_{21} & \ddots & & \vdots \\ \vdots & & \ddots & K_{56} \\ K_{61} & \cdots & K_{65} & K_{66} \end{bmatrix} \begin{bmatrix} \Delta x \\ \Delta y \\ \Delta z \\ \Delta \theta \\ \Delta \psi \\ \Delta \phi \end{bmatrix}. \tag{2.19}$$

Unfortunately, OpenSim does not currently have such capabilities. However, with the use of the SimBody [94] toolkit, and a development plugin, this type of mobilizer may be possible. Currently, an option that exists is the use of the BushingForce set within OpenSim. This BushingForce allows the definition of 6 stiffnesses, which lie in the direction of primary motion (essentially the diagonal components of the stiffness matrix K).

2.5 Muscles

The definition of muscle actuators is straightforward, but has strong capabilities in customization and complexity. In general a muscle is defined by two points, each on a separate rigid body in the BodySet. If these points are *fixed* points, which they are by default, then these muscles stay fixed within the rigid bodies' coordinate system. In other words, these points transform under the same spatial transform of the body as explained by Eq. 2.14. These muscle points can be specified explicitly by their {x,y,z} coordinates if known, or can be picked graphically relative to some bone geometry using the GUI.

2.5.1 Intermediate Muscle Attachment Points

One advantage to using OpenSim is its nice implementation of intermediate muscle points as fixed points, via points, or moving points. This capability allows for more physiologically correct muscle modeling. For example, if it is known that the muscle will pass through bone geometry, one can implement an intermediate point to avoid such non-physiologic motion.

- A **fixed** intermediate point is simple. It is fixed to some rigid body in the model, which could be any rigid body at all. The point would transform with the body's coordinate system. The muscle's line of action would then be the shortest straight distance between the three muscle points.

- A **via** point is similar to a fixed point, except that one is able to define the via point for only a specific range of motion. For example, say you only want the extra intermediate point to exist in the range of $30 - 50\,^{\circ}$ of knee flexion. A via point allows this. The

point is nonexistent outside this coordinate range, and acts like a fixed point within this range.

- A **moving** point is a point whose coordinates in the body's frame of reference are some user defined functions of some joint coordinates, and not just simply fixed.

Fig. 2.6 shows an example implementation of the fixed points used while modeling the erector spinae in our model.
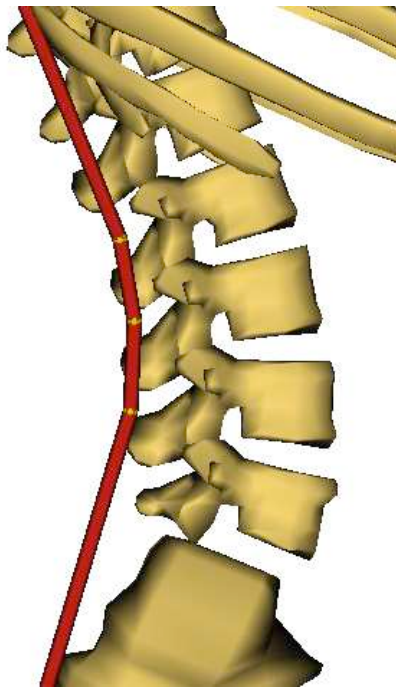
Figure 2.6: *An example of fixed intermediate points (shown as yellow points) used for the longissimus thoracis pars thoracis in the lower back. Each point is attached to the lumbar vertebra at its level.*

2.5.2   Muscle Wrapping

Muscle wrap surfaces are another way to ensure physiological lines of action. A wrap surface is also a simple yet powerful implementation. The user defined the type of geometric wrap shape they would like to use (spheres, ellipsoids, cylinders, or torii), its geometric parameters, and define the wrap objects location within a rigid body. This surface is then considered fixed within the body's coordinate frame, and again transforms with it via the same axes of rotations. The user then defines which muscles they would like to wrap on these wrap objects.

If the straight-line path of a muscle intersects a wrap object, an algorithm calculates a new path between the two points to wrap smoothly over the object. OpenSim uses two new wrap points: one at the tangent point where the muscle initiates contact, and another where it breaks contact. The muscle then follows the surface of the object between those points. There are three types of wrapping methods used in OpenSim. The reader is directed to their documentation on the topic for more details [3].

There are advantages and disadvantages to wrap objects. The advantage is that they are simpler to implement if the model has several muscles that need to wrap against such a surface. In addition, the surfaces provide smooth and physiological lines of action which make sense. The disadvantages are that the computational time of the program is increased dramatically if there are many wrapping muscles, and that the muscles may "jump" off the wrapping surfaces and cause problems. Figure 2.7a shows an example where a cylinder was used to imitate the wrapping of the erector spinae in the lower back, and Fig. 2.7b shows the moment arm produced by that muscle during a flexion-extension motion.

(a)   (b)
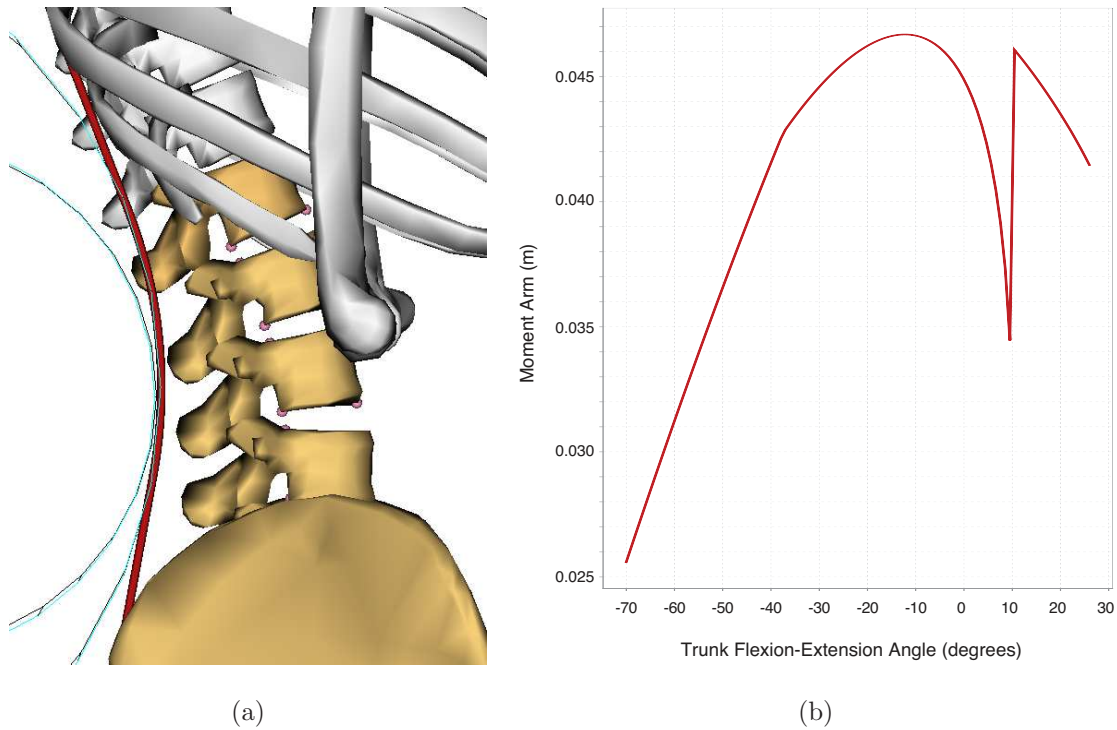
Figure 2.7: *a) An example of a cylindrical wrapping surfaces (in cyan) used for the iliocostalis lumborum pars thoracis in the lower back. b) The moment arm of this muscle as a function of flexion-extension. Note the spike in the moment arm due to the muscles jump off the surface.*

The drastic spike in the moment arm is due to a "jump" of the muscle off of the wrapping surface. The issue here is that the curvature of the spine increases (the radius decreases) as the body extends. However, the wrap cylinder keeps a constant radius during the motion. This causes the muscle to "jump" off the surface. Since OpenSim calculates the moment arm as $\Delta L/\Delta \theta$, this jump causes a falsely-large moment arm calculation.

2.6 OpenSim Toolbox

OpenSim uses a dynamics engine known as SimBody, based on the work by Schwieters and Clore [94]. This a multibody dynamics toolkit that employs the necessary spatial tranformations in order to run the simulations and the GUI manipulation in OpenSim. OpenSim has a powerful toolbox that can be used to run dynamic simulations and gain insights on experiments. The following tools are helpful for researchers around the world to input their own types of marker data, or joint torque measurements into the program, while OpenSim can then output the muscle forces and excitations, as well as kinematics required to perform such tasks. These tools represent the strong computational capabilities of OpenSim.

2.6.1 Inverse Kinematics

The Inverse Kinematics tool is provided as an interface and solution to converting marker data from a Motion Capture system to actual joint coordinate values as a function of time. The only work needed from the user is to work on scaling the marker data from the MoCap system to the musculoskeletal model in OpenSim. This includes geometric scaling as well as scaling of mass and height of a specimen.

2.6.2 Inverse Dynamics

The Inverse Dynamics tool is designed to take in a motion file, which fully defines each joint coordinate as a function of time, and uses an algorithm to determine joint forces and torques needed to create such a motion. This tool is described in further detail by Buchanan [17].

2.6.3 Static Optimization

Static optimization tool takes in as an input the motion file, and the joint forces and torques, and uses a static optimization algorithm to determine the muscle forces and activation patterns in order to keep static equilibrium of the model.

2.6.4 Computed Muscle Control

The Computed Muscle Control (CMC) tool is used to compute muscle excitations that will drive a model to track a set of desired kinematics, as specified by the kinematics input [101]. The user inputs initial states (initial joint angle, velocities, muscle activation levels and fiber lengths) into the CMC tool, and the CMC uses a combination of PD control and static optimization to determine muscle excitations. The details of the CMC algorithm and its use during forward dynamics, see Thelen *et al.* [101]. What is important here is the need to add reserve actuators to the model in case the muscles are not strong enough to track the motion. The values of these reserve actuators are a good indicator of whether the muscle is strong enough or not.

2.6.5 Forward Dynamics and RRA

The Forward Dynamics Tool drives a dynamic solution given the inputs of the CMC muscle excitations. It has been shown that using CMC to drive forward dynamics has produced high accuracy at remarkable computational speeds [100]. One may also choose to input their own excitations from experiment, or input their own external forces if they are known. A 5th order Runge-Kutta-Feldberg integrator is used in an open-loop system,

and provides kinematics. Ideally, these kinematics would match the motion file specified during CMC. However, since this is an open-loop system, the trajectory may deviate in longer simulations due to error propagation. Residual Reduction is an algorithm used to minimize the effect of marker data error and modeling error that may lead to substantially large residual forces that are non-physical (up to 50% of body weight). During a motion such as gait, the laboratory would measure a ground reaction force. In order to equilibrate this reaction force, the tool creates residual actuators, which provide extra forces and torques to balance Newton's Second Law. In order to reduce these residual forces, the Residual Reduction Algorithm makes slight adjustments to the torso's center of mass, as well as slight rotations and translations to otherwise "welded" joints, which may then have an effect of balancing Newton's second law with minimal need for residuals.

Chapter 3

Musculotendon Actuators

3.1   A Hill-Type Model

Muscle-tendons act as force generating spring and damper systems. Their force-generating capacities can be described in various ways. In the literature, a Hill-type model [43, 116] has been widely accepted to estimate tendon and muscle force. This model is composed of one non-linear spring (representing the tendon) attached to an active contractile element in parallel with a passive elastic spring (see Fig.3.1a). Anatomically, a pennation angle is sometimes seen between the muscle and tendon (see Fig. 3.2). In order to familiarize the reader with some of the variables, terms, and notation used in this section, please refer to Table A.1 in the Appendix.

For the purpose of modeling the muscle, algorithms refer to the force-length, and force-velocity curves of the muscle. A typical, normalized force-length can be seen in Fig. 3.1c. The force-length curve of the musculotendon actuator must then be scaled by a few factors: maximum isometric force (F_o^M), optimal fiber length (ℓ_o^M), and tendon slack length (ℓ_s^T).
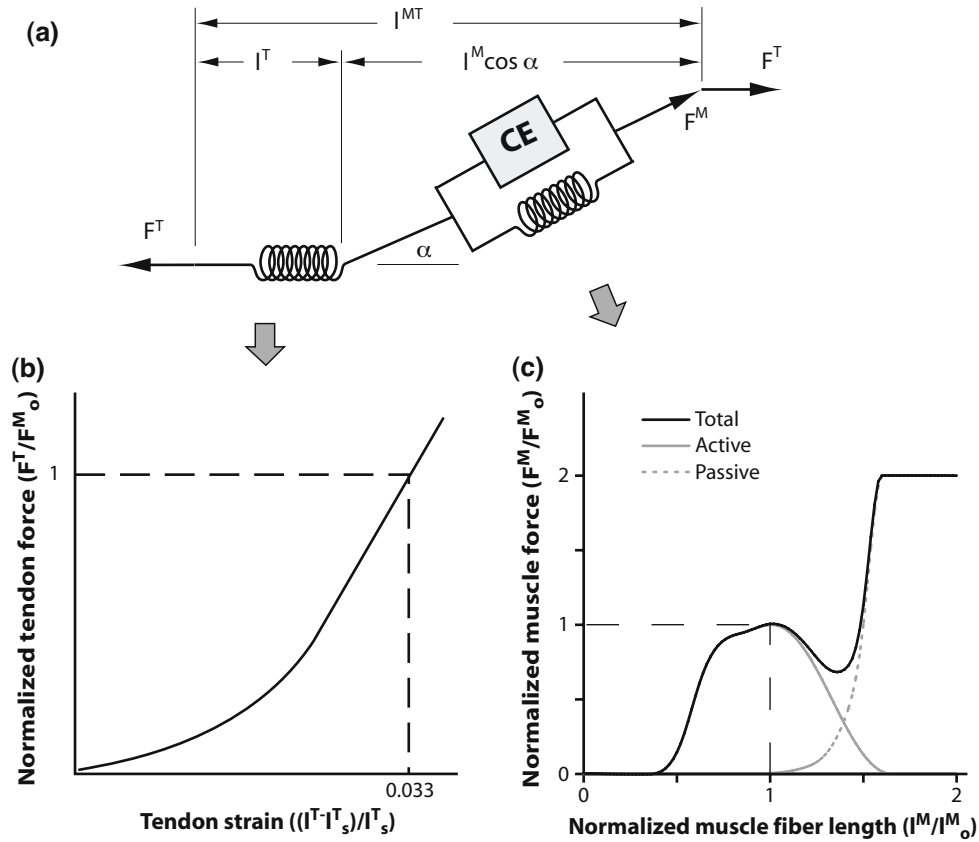
Figure 3.1: *A Hill type muscle model used to represent the force generating capacity of a musculotendon actuator. a) The mechanical model. b) A normalized representation of a tendon's force vs. strain curve. c) A normalized muscle force-length curve. Image from Arnold et al. [8].*

3.2 Thelen's Muscle Model

In 2003, Thelen [99] modified the muscle model created by Delp *et al.* [24] in order to be able to make age-based changes. For this reason, Thelen simplified the model into a Gaussian portion, and an exponential portion [99]. The active force-length relationship is given as the following Gaussian function:

$$f_l = e^{-(\overline{L}^M - 1)^2/\gamma} \tag{3.1}$$
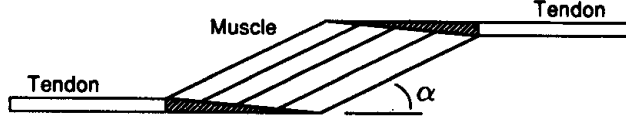
Figure 3.2: *A representation of a musculotendon with parallel muscle fibers which insert on the tendon at the same pennation angle α. Notice that the total tendon length includes the free tendon and the aponeurotic tendon (the stippled) area. Image from Hoy [44].*

where f_l is the normalized force F^M/F_o^M, and $\bar{L}^M$ is the normalized muscle length, and γ is a gaussian shape factor. According to Gordon *et al.*[36], a value of 0.45 for γ approximates the force-length relationship of individual sarcomeres well.

The passive force-length relationship is given as an exponential function:

$$\bar{F}^{PE} = \frac{e^{k^{PE}(\bar{L}^M-1)/\varepsilon_0^M} - 1}{e^{k^{PE}} - 1} \qquad (3.2)$$

The force-length curve is also assigned a particular shape factor which determines it's general shape distribution. The advantage of this muscle model is it's ease of adaptability depending on age and other specific parameters. In addition, this model is parametrically defined. The disadvantage is whether this approximation is as accurate as the Delp model presented in Sec. 3.1.

Thelen also presents a parametric equation to model the force generated due to tendon strain. He uses an exponential function for an initial region, and then by a linear function afterwards:

$$\bar{F}^T = \begin{cases} \frac{\bar{F}_{toe}^T}{e^{k_{toe}}-1}(e^{k_{toe}\varepsilon^T/\varepsilon_{toe}^T} - 1); & \varepsilon^T \leq \varepsilon_{toe}^T \\ k_{lin}(\varepsilon^T - \varepsilon_{toe}^T) + \bar{F}_{toe}^T; & \varepsilon^T > \varepsilon_{toe}^T \end{cases} \qquad (3.3)$$

The value for the non-linear stiffness used is $k_{toe} = 3$, and the assumption here is that

27
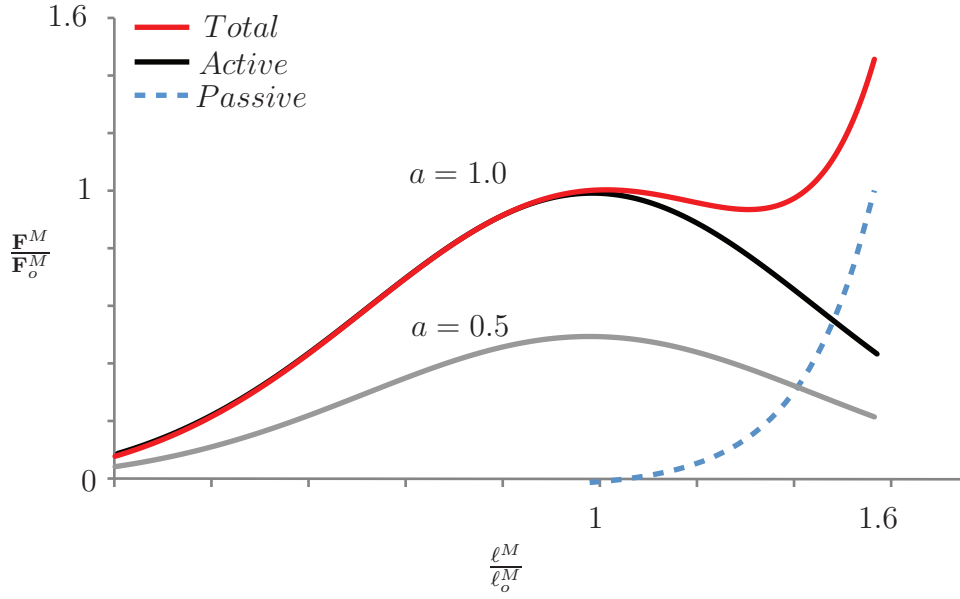
Figure 3.3: *A Thelen type muscle model based on a Gaussian distribution for active muscle force, and an exponential function for passive muscle force. It is assumed that activation, shown as a, scales the active part of the force-length curve.*

the transition from linear to non-linear occurs at $\bar{F}_{toe}^{T} = 0.33$. To maintain continuity at the transition region, Thelen determined the transition strain, ε_{toe}^{T} to be $0.609\varepsilon_{0}^{T}$, and the stiffness k_{lin} to be $1.712/\varepsilon_{0}^{T}$ [99].

The advantage to using Thelen muscle models is that making age-based changes are simpler and more transparent. For example, Table 3.1 gives a summary of the parameter adjustments between young (age 30) and old (age 70) musculotendon models.

Table 3.1: *Musculotendon parameters adjusted to reflect nominal changes in muscle mechanics occuring between the ages 30 and 70. Table from [99].*

	τ_{deact} (ms)	V_{max}^M (L_0^M/s)	ε_0^M	$\bar{F}_{len}^M$
Young	50	10	0.6	1.4
Old	60	8	0.5	1.8

Chapter 4

Lumbar Spine Muscle Architecture

Even with Zajac and Hill's notable work in the simplification and mathematical model of musculotendon actuators, the problem remains with determination of the necessary parameters (F_o^M, ℓ_o^M, α, and ℓ_s^T) [43, 116]. Unfortunately, these parameters are non trivial to attain and rely on detailed anatomical studies, assumptions, and estimation algorithms [32]. The muscle architecture data for all 238 muscle fascicles is presented in the Appendix in Table A.2.

4.1   Anatomy and Morphology

The lower back musculature consists of 9-10 muscle groups, depending on how they are viewed. Arjmand *et al.* argue that 7 primary groups are necessary for a biomechanical model of the lumbar spine. de Zee *et al.* [22, 41] ignores the transverse abdominis (TA), as it has been shown that this group only acts to produce inter-abdominal pressure (IAP), and since IAP is not modeled, it is not necessary to model the TA muscle group. However,

Cholewicki and McGill [19] have shown that intra-abdominal pressure is a mechanism for the stabilization of the spine. For this reason, we plan to model IAP in the model in the future.

4.1.1   Erector Spinae

The erector spinae is the broadest and largest muscle group in the lower back. Gray describes it has a "large fleshy mass which splits, in the upper lumbar region into three columns, viz., a lateral, the iliocostalis, an intermediate, the longissimus, and a medial, the spinalis [38]." Bogduk, performed an anatomical study in 1980 to reappraise the anatomy of the lumbar erector spinae [11]. Bogduk describes the human lumbar erector spinae as two muscle groups: "the longissimus thoracis and the iliocostalis lumborum. Furthermore, each of these muscles has two components: a lumbar part, consisting of fascicles arising from lumbar vertebrae, and a thoracic part, consisting of fascicles arising from thoracic vertebrae or ribs [12]." we will be implementing the model of the erector spinae as described in detail in [14], [62], and [61]. Following this description, the four parts of the lumbar erector spinae are: longissimus thoracis pars lumborum, longissimus thoracis pars thoracis, the iliocostalis lumborum pars thoracis, and iliocostalis lumborum pars lumborum.

4.1.1.1   Longissimus Thoracis

The longissimus thoracis pars lumborum is comprised of five fascicles, each originating from a narrow area on the ilium and insert into the adjacent medial end of the dorsal surface of the transverse process of a lumbar vertebrae (see Fig. 4.1a). The fascicles from the L1 to L4 vertebrae converge into the lumbar intermuscular aponeurosis (LIA).

31
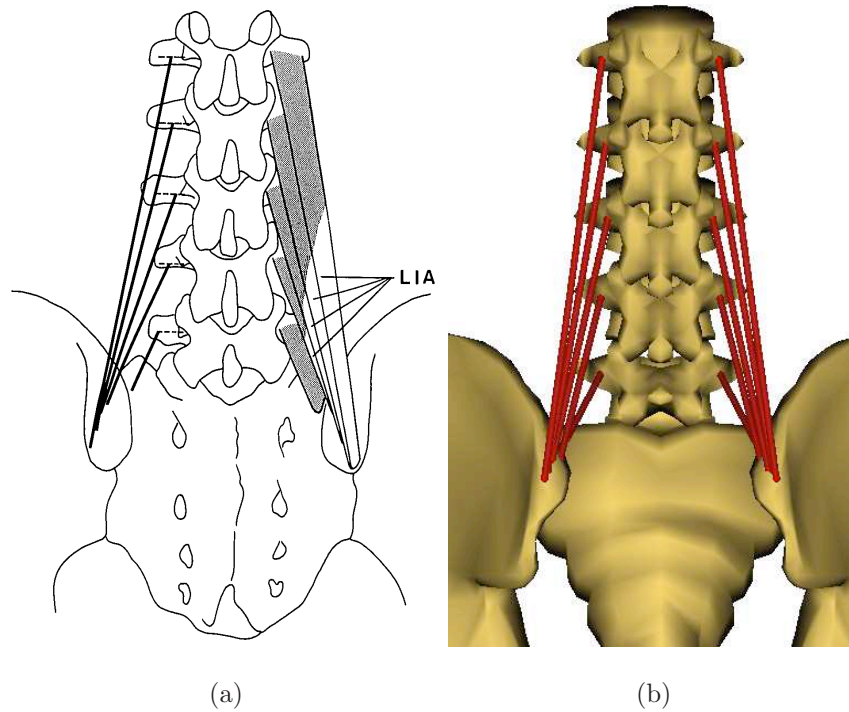
Figure 4.1: *An illustration of the fascicles of the longissimus thoracis pars lumborum. a) The L1-L4 have long caudal tendons which form the LIA. Image taken from [61] b) as modeled.*

The line of action of this lumbar portion of the longissimus can be resolved into its vertical (y), posteroanterior (z) and sagittal (x) components. The large vertical vector of the longissimus depicts that upon contraction, it can laterally flex the lumbar vertebrae. It can also act as a posterior sagittal rotator, but because its line of action lies close to the center of rotation, it is not quite efficient at this type of movement. It can also be seen that during flexion, the longissimus acts to resist anterior translation.

The thoracic portion of the longissimus is the longissimus thoracis pars thoracis. These thoracic fibers originate from the ribs and the transverse processes (tp) of T1 down to T12, and insert into the spinous processes (sp) of the lumbar vertebrae. For example, the fascicles

from the T2 tp attach to the L3 sp, and those from T5 attach to L5, while those from T7 to S2 or S3.

(a) (b) (c)
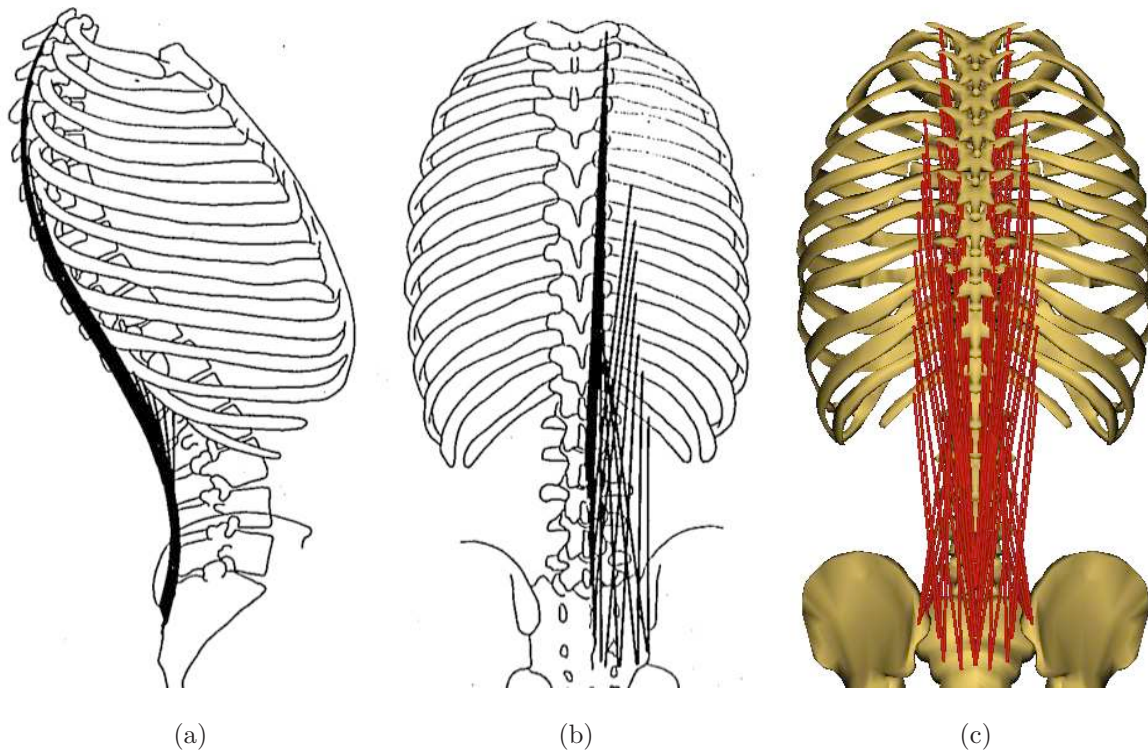
Figure 4.2: *The longissimus thoracis pars thoracis. a) a left lateral view emphasizing the wrapping characteristic of the thoracic fibers at the ribcage and the lower back. b) a posterioanterior view showing the the angular disposition of the costal fibers. Image taken from [62]. c) as modeled*

Together, the longissimus thoracis pars thoracis is designed to act on the thoracic spine and ribs. However, it indirectly acts on the lumbar vertebrae during flexion and extension, as well as a small contribution to lateral bending, due to its oblique orientation.

4.1.1.2 Iliocostalis Lumborum

The iliocostalis lumborum pars lumborum is comprised of four fascicles from the tip of the transverse processes of the L1 to L4 vertebrae to the iliac crest (see Fig. 4.3).

(a)   (b)
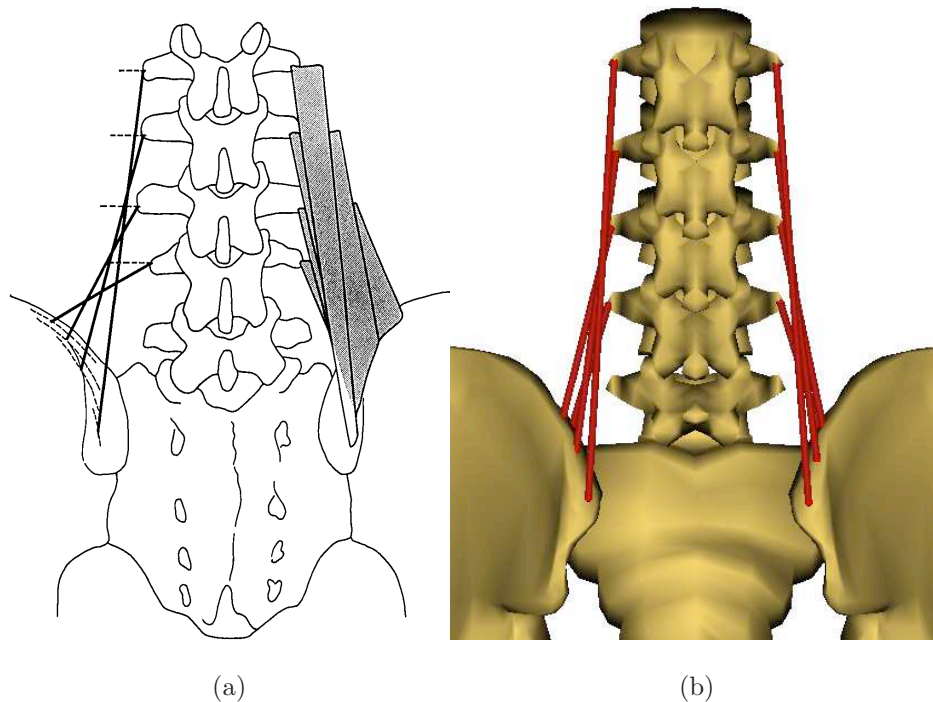
Figure 4.3: *The iliocostalis lumborum pars lumborum. a) Image from Bogduk and Macintosh in [61]*

The fascicles of the iliocostalis are better at producing axial rotation than the longissimus, as their attachment to the tips of the transverse process increases their moment arms on the axis of rotation. The iliocostalis lumborum pars thoracis (ILpT) attaches from the lower eight ribs via a thick rostral tendon across the length of the iliac crest via a caudal tendon, which composes much of the erector spinae aponeuorosis (ESA)[61]. Our model's attachment points follows the description of the 8 muscle fascicles by Macintosh and Bogduk [62]. This

description includes wide attachment locations on the iliac crest, and therefore, the centroid of these lines was chosen as an appropriate fascicle origin.

(a)   (b)
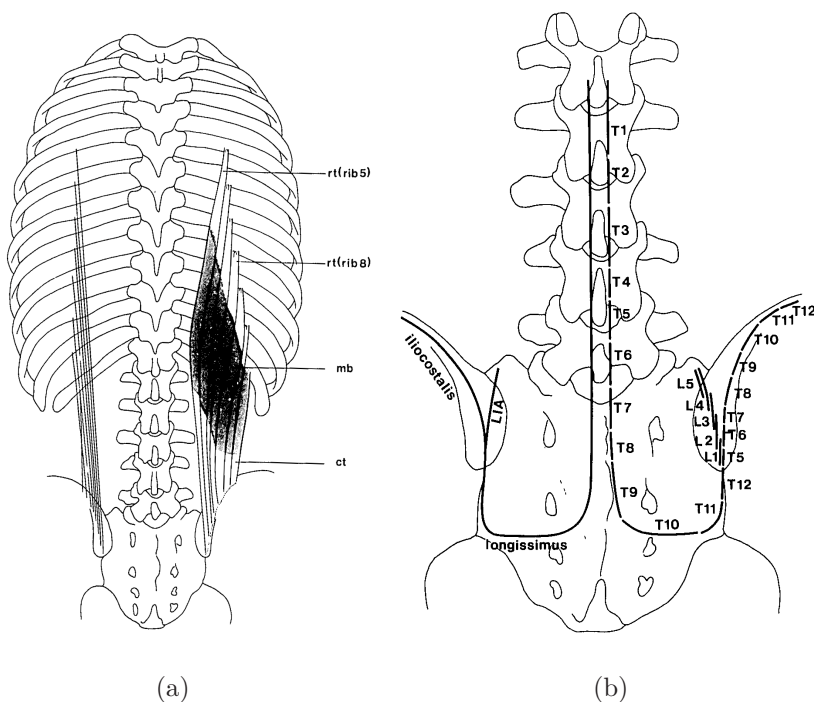
Figure 4.4: *a) The iliocostalis lumborum pars thoracis. b) The attachment points of the thoracic portions of the iliocostalis and the longissimus. Images from Macintosh and Bogduk [61].*

4.1.2   Abdominal Muscles

The abdominal muscles are global muscles, responsible as primary flexors of the lumbar vertebrae, as well as axial rotators. The abdominal muscles that are necessary for such a musculotendon model are the rectus abdominis, the external obliques and the internal obliques. Generally, these muscles have each been modeled by two lines of action (one for the right side, and another for the left). However, Stokes and Gardner-Morse's [97]

reassessment gave a more detailed description of the external and internal oblique muscles. Using transverse section photographs from the Visible Human Project and two dissected cadavers, they modeled the obliques with six fascicles each. This description is used in our model.

The external obliques are the most superficial of the muscles. Its fascicles all arise from the lower 8th to 12th ribs and attach to the Iliac crest, either directly or via the inguinal ligament [97]. Its line of action is designed well as a rotator of the thoracic spine and ribcage.

(a) (b)
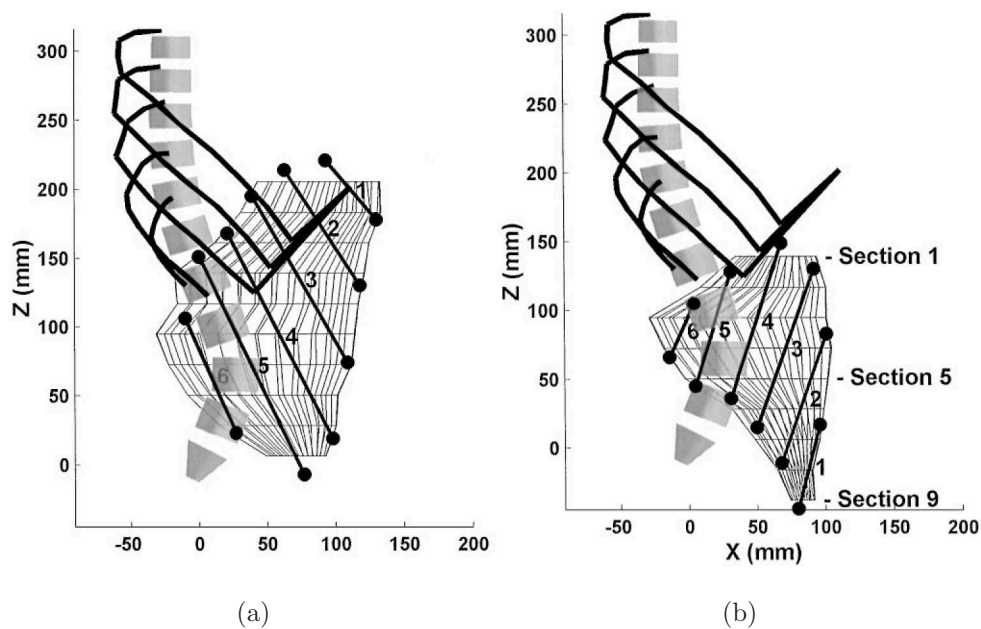
Figure 4.5: *a) The six fascicles of a) the internal oblique muscles and b) the external obliques. Image from Stokes and Gardner-Morse [97].*

The internal obliques have an almost perpendicular line of action to the external obliques, see Fig. 4.5. They directly beneath the externals, and originate from the thoracolumbar

fascia and Iliac crest and insert into the abdomen, and up to the 10th-12th ribs and sternum. Its line of action is well suited for lateral bending as well as rotation.

The rectus abdominis is responsible for the flexion of the lumbar spine, and along with the erector spinae, is considered the primary mover of the spine. Gray describes it as, "a long flat muscle, which extends along the whole length of the front of the abdomen, and is separated from its fellow of the opposite side by the linea alba [38]." He describes its line-of-action by explaining that its ligaments attach from the crest of the pubis to the cartilage of the 5th-7th costal ribs and the xiphoid process of the sternum (see Fig. 4.6a). Dumas *et al.* confirm this anatomical description and recommend modeling it as 3 fascicles [27]. Yet, for the sake of simplicity, we follow the description of the rectus abdominis as modeled by Stokes and Gardner-Morse, and Wilkenfeld *et al.* [97, 112].

<div align="center">(a)   (b)</div>
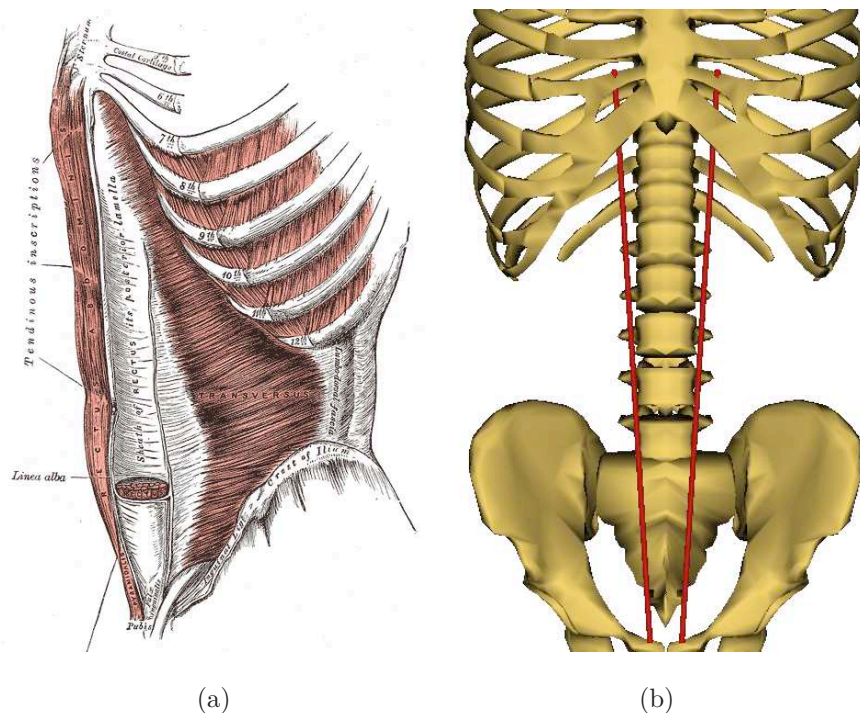
Figure 4.6: *The rectus abdominis muscle a) as depicted and described by Gray. Image from [38]. b) as modeled with two lines of action.*

In modeling the rectus abdominis, there was a significant amount of consideration towards wrapping its fascicles outward against an abdomen (represented by an ellipsoid). However, after experiencing incorrect moment arm calculations as well as the muscles jumping off of these surfaces during extension motions, they were removed. If a more suitable wrapping method is arrived at, and ensures more accurate moment arms, they will be considered.

4.1.3 Psoas Major

The psoas major was studied in great detail by Bogduk and Pearcy in 1992 [15], and Santaguida and McGill in 1995 [92]. The morphology of the psoas major consists of fleshy

fibers from the transverse processes or intervertebral discs of the lumbar vertebrae and attach via a common tendon to the femur [15]. Fig. 4.7a presents a good anatomic description of the lines of action of the psoas major, and its attachment sites on the vertebral column.

The psoas' main role is as a flexor of the hip [38]. Yet, EMG studies dated as far back as 1966 show psoas activity during forward bending, lifting and upright standing [76], [77]. This implies the role of the psoas as a stabilizer for the lumbar spine. According to Bogduk *et al.*, due to its relatively small moment arms, the psoas has no substantial role as a flexor or extensor of the lumbar spine, yet it exerts large compression and shear forces on the lumbar joints [15]. A study in 1991 by Janevic *et al.* reveals that this large compression force helps to increase spinal stiffness and thus provide lateral stability [48]. Lastly, Santaguida *et al.* firmly state that the psoas cannot act as a 'derotator' of the spine, nor can it control spinal posture, but has the moment arm to cause lateral flexion, and stabilize via compression [92]. For this reason, we have included the psoas major to further understand and confirm its action on the lumbar spine, as well as its ability to stabilize the spine by increasing spinal stiffness.

(a)   (b)
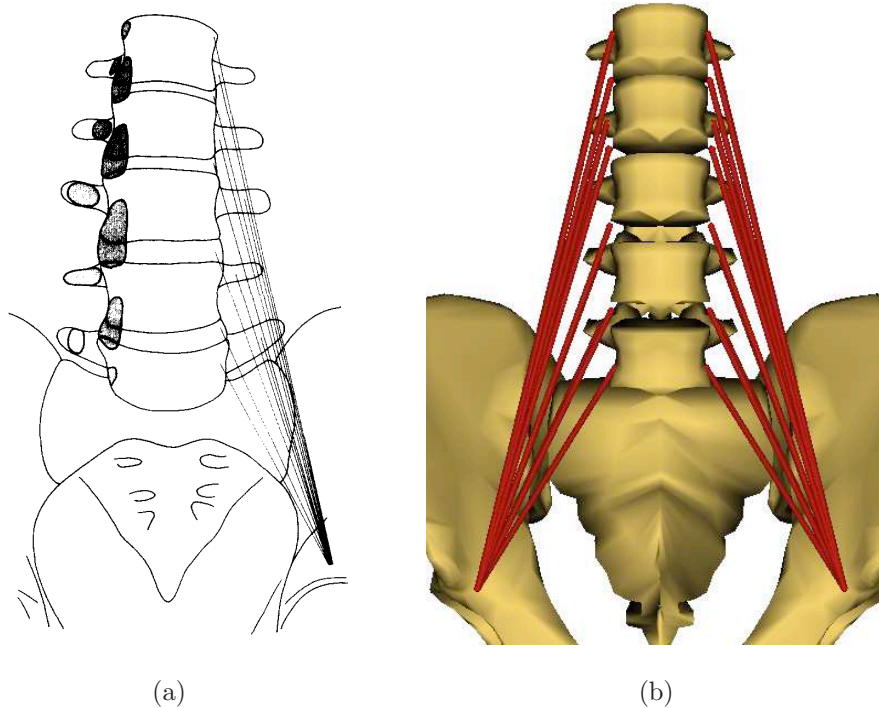
Figure 4.7: *The psoas major muscle. a) The sites of attachment: shaded areas (left) and lines of action (right) of the psoas major at the lumbar level. Image taken from Bogduk et al. [15]. b) as modeled.*

4.1.4   Multifidus

The multifidus' purpose has not been fully understood. According to EMG studies, it appears to be active during all motions of the lumbar spine. Gray describes it as a contralateral rotator of the spine [38]. In general, it is viewed as a stabilizer of the lumbar spine [59, 56, 89, 108, 109, 108]. Following the description by Macintosh *et al.*, "the principal fascicles of the lumbar multifidus arise from the lateral surface of the caudal edge of the spinous process...the caudal attacments of these fascicles are to the mamillary processes [of

the vertebra directly below] and to certain areas on the iliac crests and the dorsal surface of the sacrum [59]." Fig. 4.8a is a representation of the morphology at the L1 vertebral level. A similar pattern is seen for levels L2-L5, yet with fewer fibers. The entire multifidus muscle group as modeled in our model, is depicted in Fig. 4.8b. From an anteroposterior

(a)   (b)
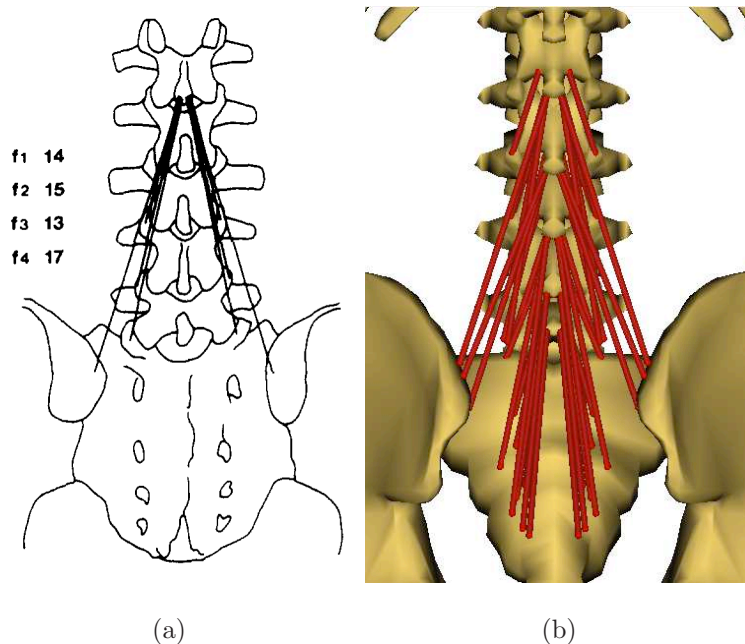
Figure 4.8: *The lumbar multifidus. a) the fibers from the L1 spinous process. Image from [59] b) the entire muscle group in our model.*

view of the multifidus, as shown in Fig. 4.8, its line-of-action can be clearly resolved into a horizontal and vertical vector. This downward action makes the multifidus effective as a posterior sagittal rotator of each vertebra. Since its fascicles are nearly perpendicular to the axes of posterior translation, it is not effective to produce any posterior shearing force. The multifidus is also commonly viewed as an axial rotator, yet Macintosh et al.'s description suits it as more of a stabilizer during rotation [59, 60]. This viewpoint is shared by Ward *et*

41

al. in their recently extensive architectural analysis of the multifidus [108].

4.1.5   Quadratus lumborum

The functions and actions of the quadratus lumborum are obscure. Its muscles connect the ilium of the pelvis to the twelfth rib and to the lumbar vertebrae. In addition, there are fascicles that attach the twelfth rib to the L3 vertebrae. In general, it is categorized into three subgroups: the anterior fibers, the middle fibers (lumbocostals), and the posterior fibers (see Fig. 4.9).

(a)   (b)
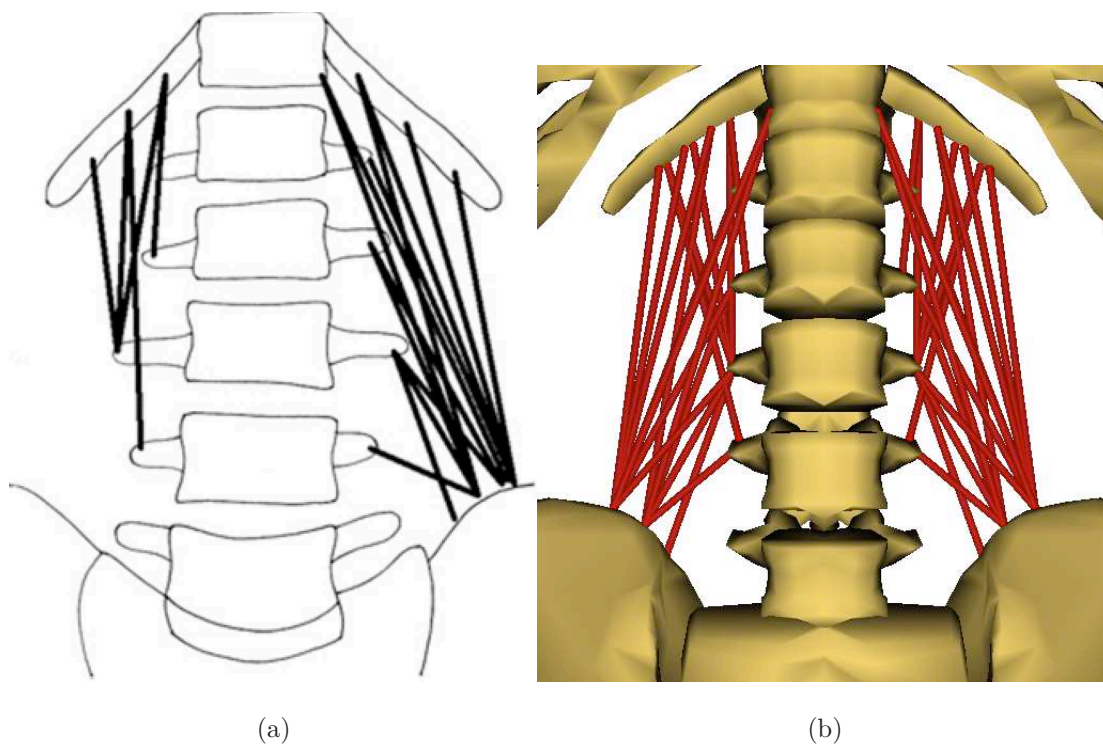
Figure 4.9: *The quadratus lumborum: a) as depicted by Phillips et al, where the right side depicts the lumbocostal fibers, and the left side, the other fibers. Image from [88] b) as modeled into our model.*

Similarly to the multifidus, researchers' EMG studies have found the quadratus lumborum to be active during a variety of lumbar motions. For this reason, it is considered to be a stabilizer of the lumbar spine, like the multifidus [67, 61, 69, 70]. A particularly mysterious characteristic of the quadratus lumborum noticed during Phillips' recent anatomical study was the inconsistency of the existence of muscle fascicles across subjects: some fascicles existed in some subjects, and not in others [88]. Following their guidance, only fascicles which existed in at least 50 percent of the subjects were modeled.

We do not expect the quadratus lumborum to exert much of a compression force on the lumbar spine. According to Phillips *et al.*'s model [88], it was only able to produce about 200N of compression force at each level, which is minimal in comparison to the erector spinae and multifidus, which are able to produce a range of 1800 to 2800N of force [14].

4.1.6 Latissimus Dorsi

The most comprehensive architectural study was undertaken by Bogduk *et al.* in 1998. They describe the muscle as "a large fan-shaped muscle covering the posterolateral aspect of the thorax. Rostrally, all of its fibres converge on a thick flat tendon that twists under the teres major to insert into...the humerus [13]." They modeled it with thirteen fascicles on each side, five from the tips of the lumbar spinous processes, six from the lower six thoracic spinous processes, and costal fibers from the 11th and 12th ribs. Fig. 4.10a gives their depiction as shown by Bogduk, and Fig. 4.10b shows the LD as modeled in our model.

It is widely known that the latissimus dorsi's morphology and activation make it primarily an adductor, extensor, and rotator of the arm. However, the latissimus dorsi's (LD)
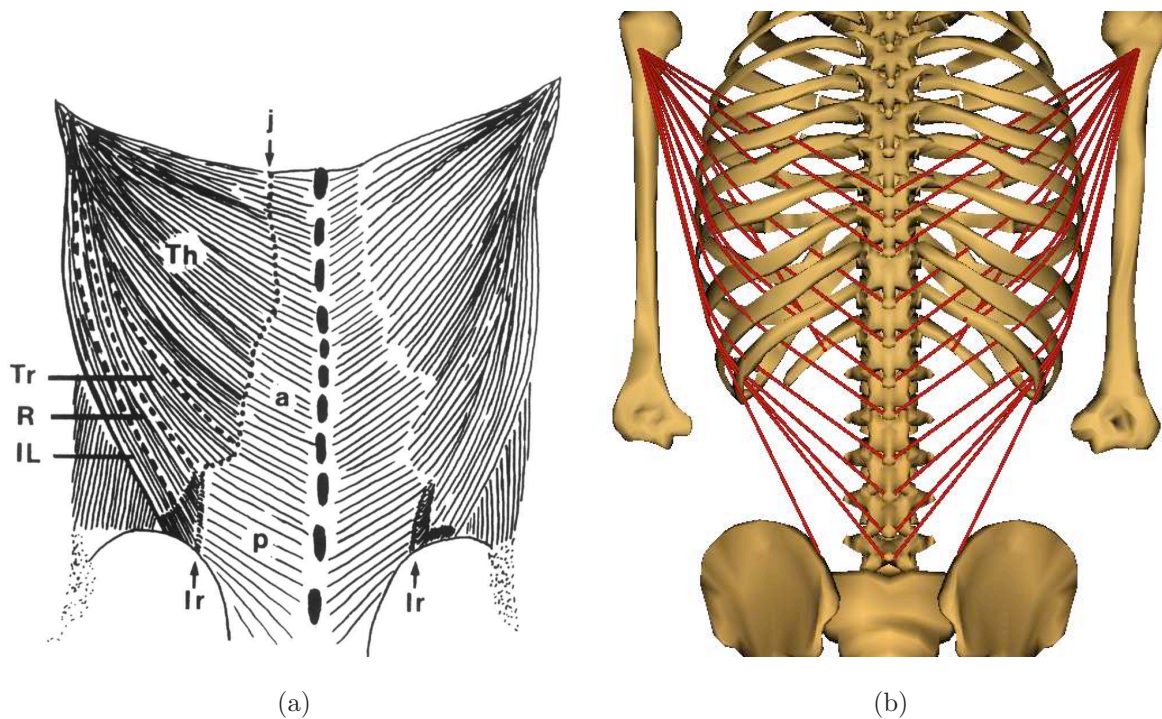
Figure 4.10: *The latissimus dorsi muscle group. a) as depicted by Bogduk et al. [13]. The dotted line j defines the transition between the muscle fibers and their tendinous aponeurosis. b) the 13 fascicles as modeled.*

attachment to the lumbar vertebra gives the impression of a non-negligible biomechanical effect on the motions of the lumbar spine. In addition, its EMG activity could imply it has a synergistic effect on the flexion of the lumbar spine. McGill and Norman concluded that the extensor moment exerted by the LD on the thoracolumbar fascia is on the order of 4% of the total moment during lifting [72]. Bogduk *et al.* confirmed these results with their model, in which the LD seemed unlikely to produce a moment exceeding 12 Nm (less than 5% of the moment required for heavy lifting) [13]. Nevertheless, its inclusion is computationally inexpensive, and hence its fascicles have been included as a study of their biomechanical

effect on the lumbar spine movements and spinal stability.

While incorporating the LD into our model, the only complexity arose in ensuring physiological wrapping around the ribcage. This wrapping was ensured by the use of two ellipsoid wrapping surfaces which were manually rotated and translated until a physiological wrapping was observed.

4.2 Physiological Cross Sectional Area

According to Panjabi, a muscle's physiological cross sectional area (PCSA), can be scaled linearly to determine its maximum force generating capacity to a first approximation. The determination of PCSA is also a topic of dispute among the literature. A basic method, used prominently by Bogduk and Macintosh during their extensive anatomical studies of the spine [11, 12, 14, 61, 62], is simply muscle volume divided by muscle fascicle length:

$$PCSA = \frac{Vol_{mf}}{\ell_{mf}} \tag{4.1}$$

Stokes and Gardner Morse use a similar algorithm, but take the pennated muscle fiber in account [97]. Others, such as Han *et al.*, use a series of Computed Tomography (CT) scans compiled to produce an estimate on PCSA [40, 45].

Due to different methods and varying subject ages, reported values of PCSA for the lumbar musculature are also inconsistent. In particular, some anatomical studies only focused on particular muscle groups, and ignored others. Therefore, data for the lumbar musculature was gathered from several sources, and was not from a cohesive set of subjects [14, 25, 88, 89, 97]. Piecing together data from several dissection studies is not ideal [8] and in order to increase accuracy and consistency, the data for muscle groups was normalized

against the erector spinae and compared to the data presented by Marras *et al.* in 2001 in an MRI study of 20 females and 10 males. Marras *et al.*'s data presents asymmetric musculature from the right to the left of the body. However, for the sake of simplicity, our model kept a symmetry from right and left sides. Table 4.1 gives a summary of a comparison of PCSA for the entire muscle group, where the data presented by our model is simply a sum of all fascicles within that group.

Table 4.1: *Comparison of previously reported PCSA (mm^2) values in lumbar spine models. Data is for a single side only. Note, the data presented here by Marras is of Males, right side.*

Muscle Group Average Age and Sex	Our Model NA	Marras[64] 26, M	Delp[25] 67, M & F	Shirazi-Adl[6] NA	McGill[66] NA, M
Quadratus lumborum	434	526	120	313	
Rectus abdominis	567	905	260	567	
Latissimus dorsi	970	2174			
Multifidus	1058			765	
Internal oblique	1345	1026		1345	1950
External oblique	1575	1006		1575	1600
Psoas	1463	1949		1374	850
Erector spinae	2788	2595	1000	3002	
Longissimus thoracis	1608		590	1709	
Iliocostalis lumborum	1180		410	1293	

The force generating capacity constant of a muscle fiber is also a topic which has not been fully agreed upon. The general relationship which has been used is:

$$F_o^M = K \times PCSA \tag{4.2}$$

However, the estimation of the Force coefficient K, has values ranging from 34-100 N/cm^2 .

Table 4.2 shows the distribution of the value of Specific Tension, K, reported in the literature. Since K determines the scaling of the force-length curve, it is a critical factor, and has a large effect on a biomechanical model. In the most recent models, a value of K in the range of 35-61 N/cm^2 is most common [8, 41, 104]. To stay consistent with our strong use of Bogduk and Macintosh's muscle data, a K value of 46 N/cm^2 was used.

Table 4.2: Range of Specific Tension values presented in the literature

Publication	Specific Tension (N/cm^2)
Bean *et al.*, 1988 [10]	22.5-38.5
Farfan, 1973 [29]	34.4
Weis-Fogh and Alexander, 1977 [110]	40
Bogduk *et al.*, 1992 [14]	46
El-Rich et al., [28]	60
Arnold *et al.*, 2000 [7]	61
Ikai and Fukunaga, 1968 [46]	62
Van Dieen and Kingma, 1999 [103]	88
Schultz and Andersson, 1981 [93]	100

4.3   Pennation Angle

Pennation Angle must also be measured by anatomical studies for determination. Delp *et al.* did a thorough study on the muscles of the erector spinae, quadratus lumborum, and rectus abdominis muscles [25]. In this study, he reported the pennation angle of these muscles as a group by taking a selection of muscle fascicles and averaging them. Our assumption is that the pennation angle for a muscle group is fairly consistent among all fascicles in that muscle group. Therefore, the pennation angles determined by Delp were used across these

muscles.

Anderson *et al.* reports that the cervical multifidus has negligible pennation angle [4]. For this reason, our model also excludes pennation angle for the lumbar multifidus. Similarly, for the latissimus dorsi muscle group, due to lack of data in the literature on pennation angle, we assumed a zero degree pennation. Ward *et al.* reported pennation angle of the psoas major in his work on the human lower extremity [8, 107].

4.4   Optimal Fiber Length

Optimal fiber length is the length at which the active muscle generates its largest force. In addition, it is the length past which passive force is developed. In order to determine optimal fiber length, an accurate measurement of the fiber's resting sarcomere length is needed, in addition to the muscle's resting fiber length. A photo-electric method for determining sarcomere length in vertebrates was developed by Gordon *et al.* in 1966 [36]. Murray *et al.* use a modern adaption of this method using laser diffraction through the muscle fiber, and measuring the pattern with a micrometer [75]. With an accurate measurement of the resting sarcomere length and then normalizing it against an optimal sarcomere length, one can scale the fiber, and get a general determination of optimal fiber length:

$$\ell_o^M = \ell^F \times \frac{\ell_o^S}{\ell^S},\tag{4.3}$$

where ℓ_o^S is the optimal sarcomere length of whichever animal is being studied, and ℓ^S is the measured sarcomere length. In humans, an optimal sarcomere length of 2.7 to 2.8 μm has been reported [25, 105, 107]. The resting sarcomere lengths for the erector spine, quadratus lumborum, and abdominal muscles were reported by Delp *et al.* [25]. Ward *et al.*'s recently

extensive studies on the multifidus and psoas major provides the sarcomere length and fiber length's of these groups [107, 108, 108]. The only data unavailable was for the latissimus dorsi group. For this group, we took an average of the back muscles, and took the sarcomere length to be $2.3\mu m$.

4.5 Tendon Slack Length

A tendon is a passive non-linear element with a relatively high stiffness (about 180 N/mm) [55]. A tendon is assumed to generate maximum isometric force at only 3.3% strain [53]. Tendon slack length is the length at which the tendon is slack (i.e. the un-stretched spring length). This parameter is also the most difficult to determine, and several studies have attempted to create algorithms for its estimation [53, 63]. Because of its large passive stiffness, the force-length curve of a musculotendon is highly sensitive to correct data. Fig. 4.11 shows how the initial slack length guess produces dramatically different moments at the knee joint.
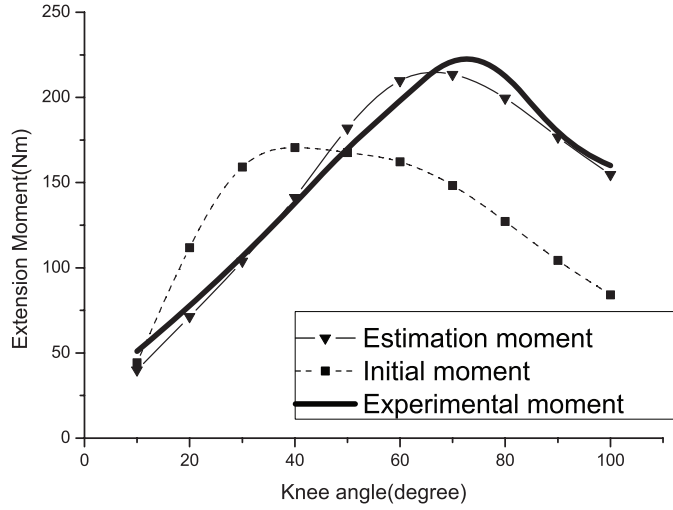
Figure 4.11: *The optimization method of determining tendon slack length by Lee et al. [53]. Note the large effect of an incorrect initial tendon slack length guess has on the knee moment.*

Since sufficient data does not exist in the literature on the tendon slack lengths of detailed fascicles of the lumbar musculature, they were estimated by generalizing the relationship between muscle length and tendon slack length in Eq. 4.4:

$$\ell_S^T \approx \ell^{MT} - \ell^f \cos(\alpha). \tag{4.4}$$

Where α is the fascicles pennation angle, and ℓ^{MT} and ℓ^f are musculotendon length and known fascicle length, respectively, at a neutral position. In releasing this model on the SimTK website, we hope that the research community will eventually supply the exact tendon slack lengths for the detailed musculature.

Chapter 5

Open Source Lumbar Spine Model and Results

In order to build this model, we began with a generic model of the torso and lower extremity created by Delp *et al.* [8, 24]. The bone geometry was created using digitized data from a male subject with a height of 170 cm. The Delp model, however, modeled the entire torso (which includes the spine and ribcage) as an entire rigid body. Therefore, creation of a lumbar model with individual vertebrae with relative movements consisted of the tedious task of the translation and rotation of each individual vertebral body to match the correct posture of the human lumbar spine.

In addition, it is important to ensure that the lordosis (curvature) of the spine is consistent with a healthy, average spine. Cholewicki *et al.* [18] conducted a study with nine cadaveric spines and reported their average posture.

More recently, Meakin *et al.* [74] conducted a study using magnetic resonance scanning of 24 male volunteers, and reported the intrinsic shape of the lumbar spine in the standing

position. This study, as well as [49], [73] an [90] all report large inter-subject variation in spinal postures. Therefore, the posture used in this model was consistent with the digitzed geometry and compared well with the published data of Cholewicki *et al.* [18] and of Meakin *et al.*. The lumbar geometry was then compared with the vertebral anatomical studies of 157 healthy young males, 20-38 years old, performed by Nissan and Gilad [34, 35, 78], as well as the examination by Panjabi *et al.* [83] and the intervertebral heights were adjusted according to the ratio of vertebral height to disc height (VBHp/VDHp).

An image of the full spine model is shown in Fig. 5.1. The final model consists of 13 rigid bodies. However, only the 5 lumbar vertebrae have dynamic mobility. In other words, the sacrum, pelvis, and femurs are welded to the ground, and the torso (thoracic spine plus ribcage) is welded to the L1 vertebra. Additionally, the five joints connecting the individual lumbar vertebrae have been modeled as 6 degree-of-freedom joints, with the axes of these transformations defined by Fig. 2.4.

At each vertebra level, it was necessary to specify the masses and moments of inertia. These values were determined from Pearsall *et al.*'s extensive examination [87] of the mass and moments of inertia at each trunk level via MR imaging. Pearsall et al. later expanded upon this work using in vivo CT scans and reported segmental data at each vertebral level [86]. The data from [86] was incorporated into the model and is presented here in Table 5.1. The locations of the IAR of each of the 5 joints was taken from the kinematic radiographic study of ten normal individuals by Pearcy and Bogduk [84]. Fig. 5.2 (cf. Fig. 9 of [84]) shows the mean of the IAR location of the ten individuals.

It is important to note that this study only examined the location of the IAR during flexion and extension of the lumbar spine. As the location of the IAR differs depending on

(a)   (b)
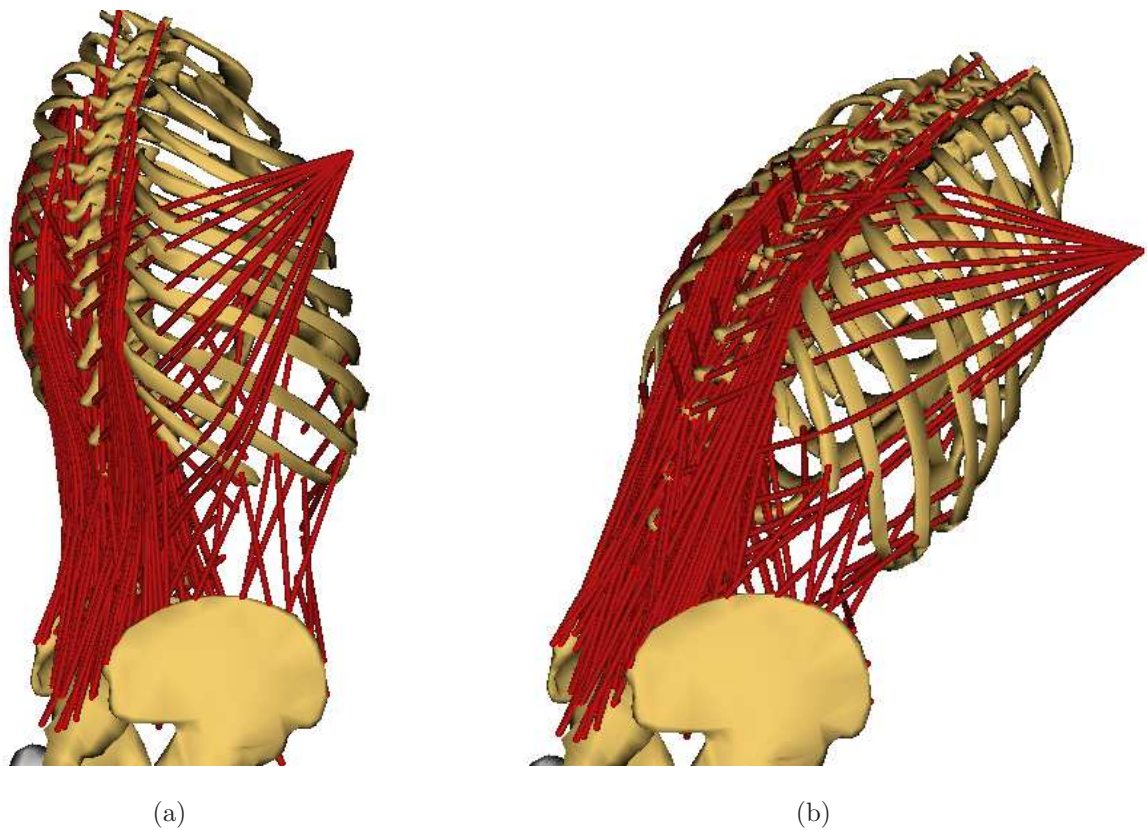
Figure 5.1: *A detailed musculoskeletal model of the lumbar spine with 238 muscle fascicles, 13 rigid bodies, and 5 intervertebral joints. a) in neutral posture and b) at* $50°$ *flexion.*

the primary motion (flexion-extension, axial rotation, or lateral bending) [9, 113] and, as suggested by Ahmadi *et al.*, the arc length pathways of the IAR is significantly longer at some vertebral levels in patients with lumbar segmental instability (LSI) [2], the ideal model would incorporate joint IAR locations that are a function of the motion. However, specifying varying joint locations depending on the motion is not easily implemented in OpenSim, and can lead to complex model structure. Furthermore, it has been shown that the determination of the IAR by planar radiographs can lead to large error propagation for finite rotations [81]. In general, this location is not well defined, and therefore, we have assumed that, as long as

Table 5.1: Mass and Inertia estimates for the Trunk, as determined by Pearsall et al. [86]

Level	Mass (g)	Trunk Mass (%)	Body mass (%)	I_{xx}	I_{yy} $(kg \cdot cm^2)$	I_{zz}
Upper Trunk	13149	44.6	18.5	1250.0	1650.0	1500.0
L1	1677	5.7	2.4	64.0	111.3	175.3
L2	1689	5.7	2.4	59.1	109.1	168.2
L3	1670	5.7	2.3	54.1	106.6	160.8
L4	1799	6.2	2.6	52.0	112.3	164.3
L5	1824	6.3	2.6	54.6	121.9	176.5
Pelvis and Sacrum	7486	25.6	10.7	300.0	750.0	800.0

the joint location lies within one std. of the mean, the ensuing kinematics are valid.

After the body geometry was arranged correctly muscle architecture was implemented according to anatomical studies as given in detail in Chapter 4. Combining all of the published anatomical muscle studies with the correct posture and joint kinematics was a much greater feat than expected due to the large number of muscle fascicles involved and the need to incorporate wrapping surfaces to ensure physiological lines of action for the muscle forces. The manipulation of the model with the GUI can become tedious.

In Fig. 5.3, we have plotted the moment produced by the two largest flexor muscle groups, the rectus abdominis and the erector spinae, for a single side. In order to obtain this for the erector spinae, all the fascicles of the iliocostalis and the longissimus were summed.

What is interesting to note here is that the moment's generated by these two primary lumbar flexors seem to balance well through the entire range of joint angles. For comparison, the contributions of the other, deeper muscles, such as the multifidus and quadratus lumborum, are plotted in Fig. 5.4. These muscles are not known to be primary flexors

<div align="center">(a)   (b)</div>
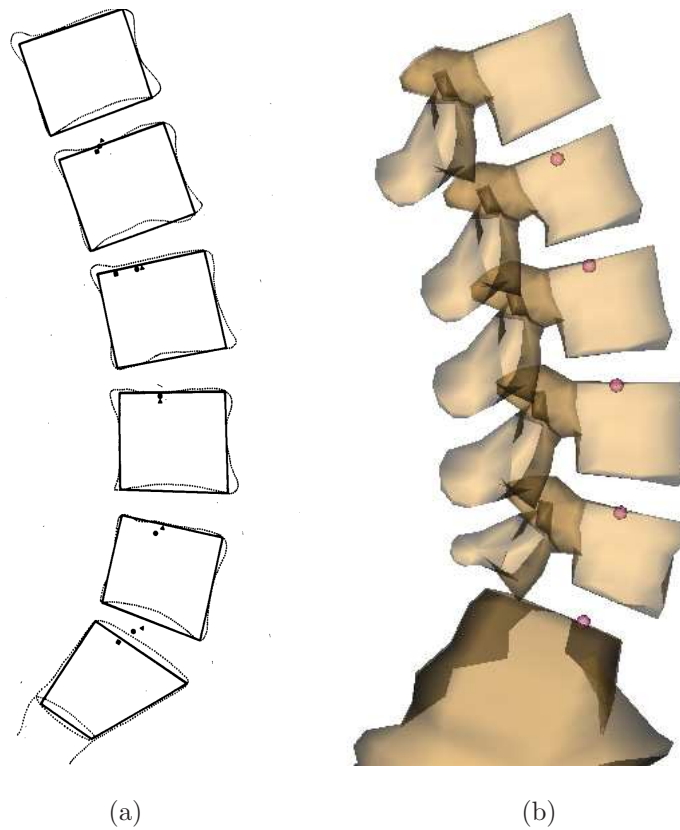
Figure 5.2: *Locations of the instantaneous axis of rotation (IAR) for the 5 lumbar interver-
tebral joints a) as determined by Pearcy and Bogduk [84] b) as modeled*

of the lumbar spine, and hence should have negligible moments at the L5/S1 joint during

flexion-extension. In comparison to the large moments produced by rectus abdominis and

erector spinae, it can be noticed that the deeper muscles only contribute up to 10 Nm during

the flexion-extension movement. This agrees well with the literature in that these muscles

serve little purpose in flexing the lumbar spine.

The purpose of this model is primarily as an analytic tool for researchers to analyze

spinal kinematics in the hopes of further improving our understanding of the pathology

and potential remedies of chronic lower back pain. Furthermore, it has been shown that
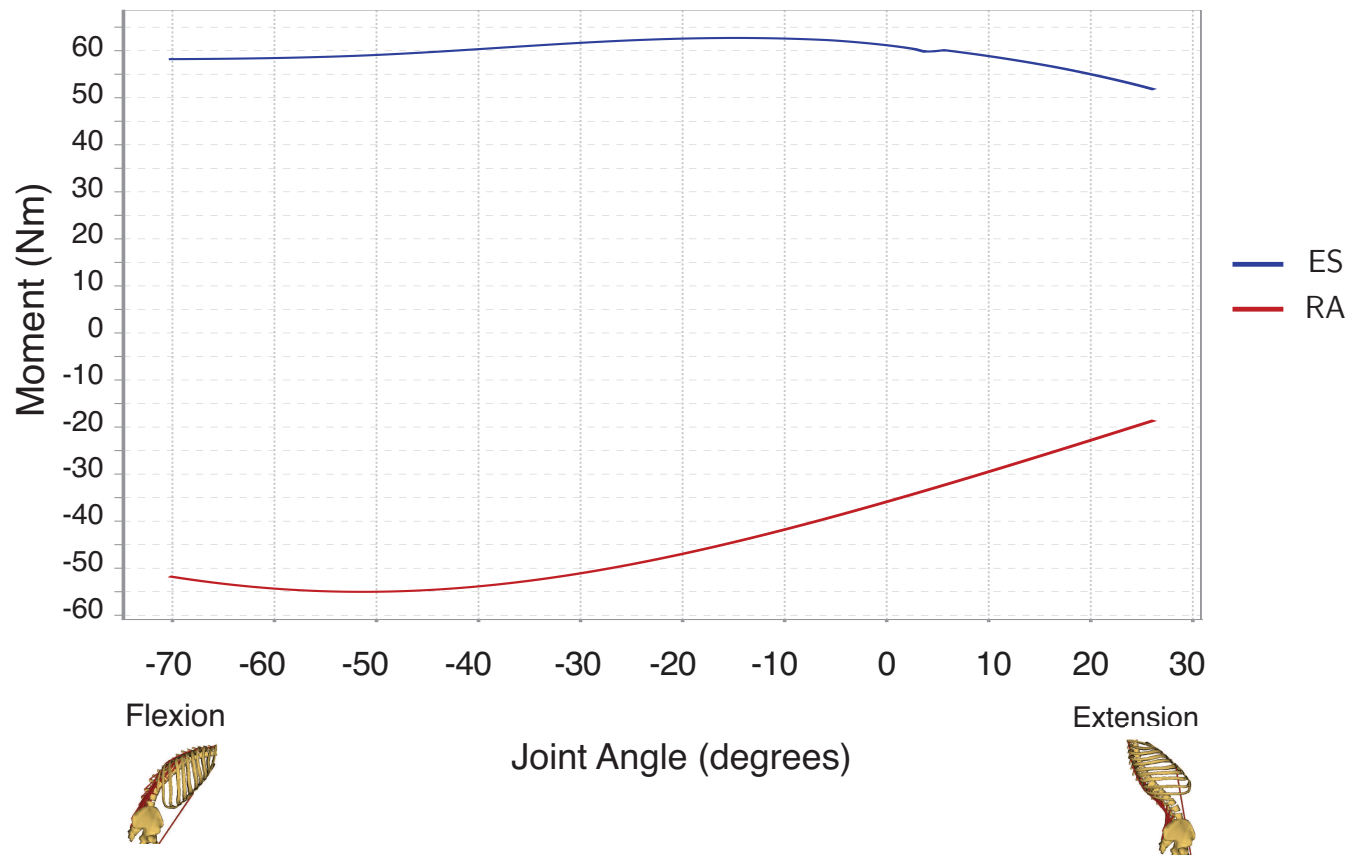
Figure 5.3: *Moment generated at L5/S1 joint by the two primary flexor muscle groups, erector spinae (ES) and rectus abdominis (RA). The erector spinae plotted here consists of a sum of the longissimus and the iliocostalis groups.*

specific muscular activation patterns are necessary to maintain spinal stability [16, 21, 28]. This model is an ideal starting point for studying the hypothesis that lower back pain is a consequence of joint degeneration in combination with altered muscle activation patterns. In particular, this model is well suited to study the phenoma of antagonistic muscle co-activation during lifting, and the concomitant affects on spinal stability.

Despite the complexity of the model, there are still a number of improvements that need to be incorporated to ensure that the model truly replicates human lumbar kinematics.
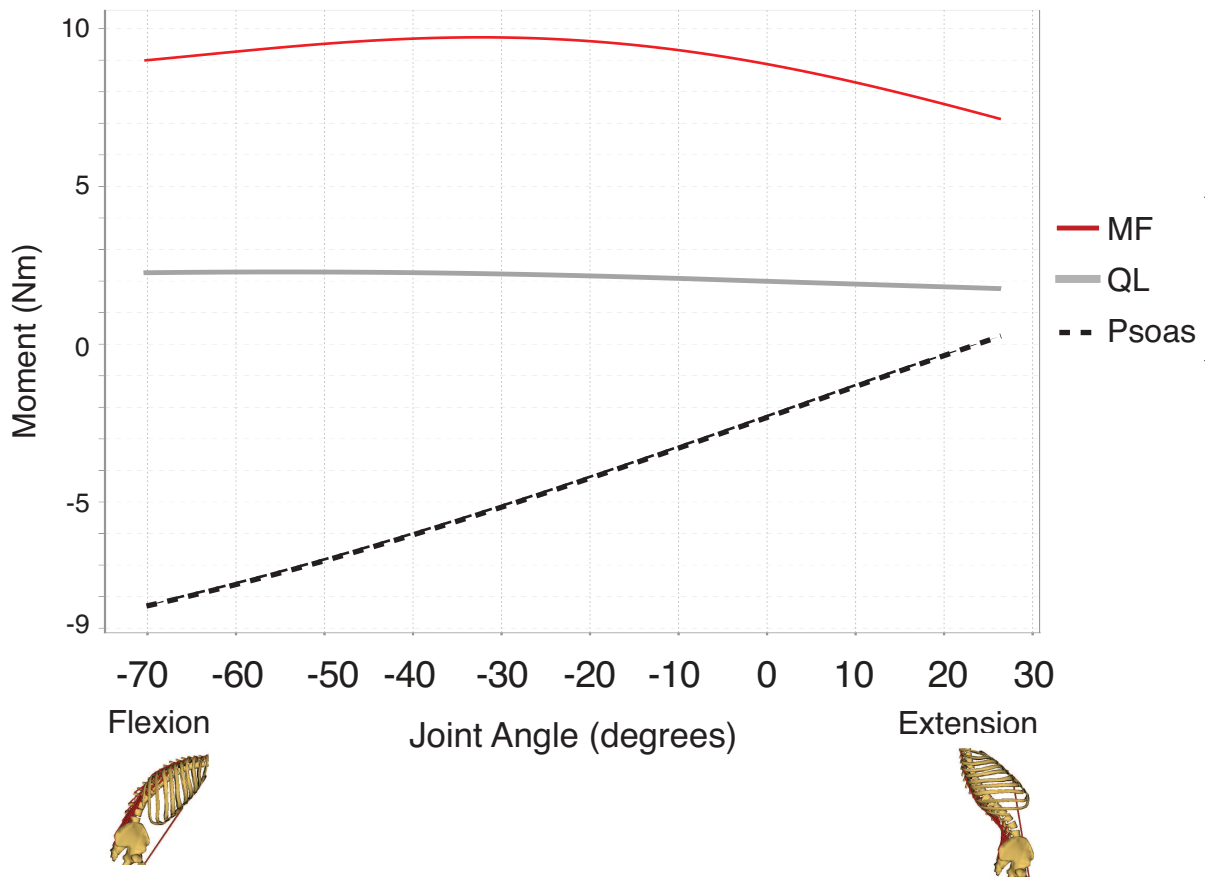
Figure 5.4: *Moment generated at L5/S1 joint by the deeper, stabilizer muscles, the Quadratus lumborum (QL), Multifidus (MF), and Psoas.*

One of the main deficiencies in the model currently is the lack of intra-abdominal pressure (IAP). As it has been shown that IAP is a mechanism for stabilizing the lumbar spine [19], a stability analysis of our model sans the incorporation of the IAP may produce skewed results. Additionally, the effects of the passive structures in the lumbar spine - the intervertebral disc,ligaments, and facet joints - have not been included thus far. These passive structures are also hypothesized to play a synergistic role with the muscles in maintaining spinal stability [37].

Nevertheless, the open-source nature of this model naturally lends itself to improvement

by the biomedical research community. It is our hope that, by making our model publicly available, the limitations mentioned above can be addressed in a relatively straightforward and effortless manner via the collaborative efforts of the OpenSim research community.

Bibliography

[1] M. A. Adams. Biomechanics of back pain. *Acupuncture in Medicine*, 22(4):178–188, 2004.

[2] A. Ahmadi, N. Maroufi, H. Behtash, H. Zekavat, and M. Parnianpour. Kinematic analysis of dynamic lumbar motion in patients with lumbar segmental instability using digital videofluoroscopy. *European Spine Journal*, 18(11):1677–1685, 2009.

[3] F. Anderson, S. Delp, C. John, A. Seth, and A. Habib. *OpenSim User's Guide: Release 2.0.1*. Simbios National Center for Biomedical Computing, February 2010.

[4] J. Anderson, A. Hsu, and A. N. Vasavada. Morphology, architecture, and biomechanics of human cervical multifidus. *Spine*, 30(4):E86–E91, 2005.

[5] G. B. J. Andersson. Epidemiological features of chronic low-back pain. *The Lancet*, 354(9178):581–585, 1999.

[6] N. Arjmand and A. Shirazi-Adl. Model and in vivo studies on human trunk load partitioning and stability in isometric forward flexions. *Journal of Biomechanics*, 39(3):510–521, 2006.

[7] A. S. Arnold, S. Salinas, D. Hakawa, and S. L. Delp. Accuracy of muscle moment arms estimated from mri-based musculoskeletal models of the lower extremity. *Computer Aided Surgery*, 5(2):108–119, 2000.

[8] E. M. Arnold, S. R. Ward, R. L. Lieber, and S. L. Delp. A model of the lower limb for analysis of human movement. *Annals of Biomedical Engineering*, 38(2):269–279, 2010.

[9] I. Augustus A White and M. M. Panjabi. The basic kinematics of the human spine. A review of past and current knowledge. *Spine*, 3(1):12–20, 1978.

[10] J. C. Bean, D. B. Chaffin, and A. B. Schultz. Biomechanical model calculation of muscle contraction forces: A double linear programming method. *Journal of Biomechanics*, 21(1):59–66, 1988.

[11] N. Bogduk. A reappraisal of the anatomy of the human lumbar erector spinae. *Journal of Anatomy*, 131(Pt 3):525, 1980.

[12] N. Bogduk and S. M. Endres. *Clinical anatomy of the lumbar spine and sacrum.* Churchill Livingstone, New York, 4th edition, 2005.

[13] N. Bogduk, G. Johnson, and D. Spalding. The morphology and biomechanics of latissimus dorsi. *Clinical Biomechanics*, 13(6):377–385, 1998.

[14] N. Bogduk, J. E. Macintosh, and M. J. Pearcy. A universal model of the lumbar back muscles in the upright position. *Spine*, 17(8):897–913, 1992.

[15] N. Bogduk, M. J. Pearcy, and G. Hadfield. Anatomy and biomechanics of psoas major. *Clinical Biomechanics*, 1992.

[16] S. H. M. Brown, F. Vera-Garcia, and S. McGill. Effects of abdominal muscle coactivation on the externally preloaded trunk: Variations in motor control and its effect on spine stability. *Spine*, 31(13):E387–E393, 2006.

[17] T. Buchanan, D. Lloyd, K. Manal, and T. Besier. Estimation of muscle forces and joint moments using a forward-inverse dynamics model. *Medicine & Science in Sports & Exercise*, 37(11):1911, 2005.

[18] J. Cholewicki, J. J. Crisco, and T. Oxland. Effects of posture and structure on three-dimensional coupled rotations in the lumbar spine. *Spine*, pages 2421–2428, Jan 2001.

[19] J. Cholewicki, K. Juluru, and S. McGill. Intra-abdominal pressure mechanism for stabilizing the lumbar spine. *Journal of Biomechanics*, 32(1):13–17, 1999.

[20] J. Cholewicki, S. McGill, and R. W. Norman. Comparison of muscle forces and joint load from an optimization and EMG assisted lumbar spine model: Towards development of a hybrid approach. *Journal of Biomechanics*, 28(3):321–331, 1995.

[21] J. Cholewicki, A. P. Simons, and A. Radebold. Effects of external trunk loads on lumbar spine stability. *Journal of Biomechanics*, 33(11):1377–1385, 2000.

[22] M. de Zee, L. Hansen, C. Wong, J. Rasmussen, and E. B. Simonsen. A generic detailed rigid-body lumbar spine model. *Journal of Biomechanics*, 40(6):1219–1227, Jan 2007.

[23] S. L. Delp, F. Anderson, A. S. Arnold, J. P. Loan, A. Habib, C. John, E. Guendelman, and D. G. Thelen. Opensim: Open-source software to create and analyze dynamic simulations of movement. *IEEE Transactions on Biomedical Engineering*, 54(11):1940–1952, 2007.

[24] S. L. Delp, J. P. Loan, M. G. Hoy, F. E. Zajac, E. L. Topp, and J. M. Rosen. An interactive graphics-based model of the lower extremity to study orthopaedic surgical procedures. *IEEE Transactions on Biomedical Engineering*, 37(8):757–767, 1990.

[25] S. L. Delp, S. Suryanarayanan, W. Murray, J. Uhlir, and R. J. Triolo. Architecture of the rectus abdominis, quadratus lumborum, and erector spinae. *Journal of Biomechanics*, 34(3):371–375, 2001.

[26] A. Deshpande and D. Riehle. The total growth of open source. *Open Source Development, Communities and Quality*, pages 197–209, 2008.

[27] G. A. Dumas, M. J. Poulin, B. Roy, M. Gagnon, and M. Jovanovic. Orientation and moment arms of some trunk muscles. *Spine*, 16(3):293–303, 1991.

[28] M. El-Rich, A. Shirazi-Adl, and N. Arjmand. Muscle activity, internal loads, and stability of the human spine in standing postures: Combined model and in vivo studies. *Spine*, 29(23):2633–2642, 2004.

[29] H. Farfan. *Mechanical Disorders of the Low Back*. Lea & Febiger, Philadelphia, PA., 1973.

[30] R. Fujii, H. Sakaura, Y. Mukai, N. Hosono, T. Ishii, M. Iwasaki, H. Yoshikawa, and K. Sugamoto. Kinematics of the lumbar spine in trunk rotation: In vivo three-dimensional analysis using magnetic resonance imaging. *European Spine Journal*, 16(11):1867–1874, 2007.

[31] M. G. Gardner-Morse and I. A. F. Stokes. Structural behavior of human lumbar spinal motion segments. *Journal of Biomechanics*, 37(2):205–212, 2004.

[32] B. Garner and M. Pandy. Estimation of musculotendon properties in the human upper limb. *Annals of Biomedical Engineering*, 31(2):207–220, 2003.

[33] E. Gercek, F. Hartmann, S. Kuhn, J. Degreif, P. M. Rommens, and L. Rudig. Dynamic angular three-dimensional measurement of multisegmental thoracolumbar motion in vivo. *Spine*, 33(21):2326–2333, 2008.

[34] I. Gilad and M. Nissan. Sagittal evaluation of elemental geometrical dimensions of human vertebrae. *Journal of Anatomy*, 143:115–120, 1985.

[35] I. Gilad and M. Nissan. A study of vertebra and disc geometric relations of the human cervical and lumbar spine. *Spine*, 11(2):154–157, 1986.

[36] A. Gordon, A. Huxley, and F. Julian. The variation in isometric tension with sarcomere length in vertebrate muscle fibres. *The Journal of Physiology*, 184(1):170, 1966.

[37] K. P. Granata. Response to "Static and dynamic stability of the spine". *Journal of Biomechanics*, 39:2921–2922, 2006.

[38] H. Gray. *Gray's Anatomy*. Warwick and Williams, London, UK, 36th edition, 1980.

[39] G. G. Gregersen and D. B. Lucas. An in vivo study of the axial rotation of the human thoracolumbar spine. *The Journal of Bone and Joint Surgery*, 49(2):247–262, 1967.

[40] J. Han, J. Ahn, V. K. Goel, R. Takeuchi, and D. McGowan. CT-based geometric data of human spine musculature. Part I. Japanese patients with chronic low back pain. *Journal of Spinal Disorders*, 5(4):448–458, 1992.

[41] L. Hansen, M. de Zee, J. Rasmussen, T. B. Andersen, C. Wong, and E. B. Simonsen. Anatomy and biomechanics of the back muscles in the lumbar spine with reference to biomechanical modeling. *Spine*, 31(17):1888–1899, 2006.

[42] D. S. Hickey and D. W. L. Hukins. Relation between the structure of the annulus fibrosus and the function and failure of the intervertebral disc. *Spine*, 5(2):106–116, 1980.

[43] A. V. Hill. The heat of shortening and the dynamic constants of muscle. *Proceedings of the Royal Society of London. Series B, Biological Sciences*, 126(843):136–195, 1938.

[44] M. Hoy, F. E. Zajac, and M. Gordon. A musculoskeletal model of the human lower extremity: the effect of muscle, tendon, and moment arm on the moment-angle relationship of musculotendon actuators at the hip, knee, and ankle. *Journal of Biomechanics*, 23(2):157–169, 1990.

[45] G. Hultman, M. Nordin, H. Saraste, and H. Ohlsèn. Body composition, endurance, strength, cross-sectional area, and density of mm erector spinae in men with and without low back pain. *Journal of Spinal Disorders*, 6(2):114–123, 1993.

[46] M. Ikai and T. Fukunaga. Calculation of muscle strength per unit cross-sectional area of human muscle by means of ultrasonic measurement. *European Journal of Applied Physiology and Occupational Physiology*, 26(1):26–32, 1968.

[47] T. Ishii, Y. Mukai, N. Hosono, H. Sakaura, Y. Nakajima, Y. Sato, K. Sugamoto, and H. Yoshikawa. Kinematics of the upper cervical spine in rotation: In vivo three-dimensional analysis. *Spine*, 29(7):E139–E144, 2004.

[48] J. Janevic, J. A. Ashton-Miller, and A. B. Schultz. Large compressive preloads decrease lumbar motion segment flexibility. *Journal of Orthopaedic Research*, 9(2):228–36, Mar 1991.

[49] T. Keller and A. Roy. Posture-dependent isometric trunk extension and flexion strength in normal male and female subjects. *Journal of Spinal Disorders*, 15(4):312, 2002.

[50] A. Kittur and R. Kraut. Harnessing the wisdom of crowds in Wikipedia: quality through coordination. *Proceedings of the ACM 2008 Conference on Computer Supported Cooperative Work*, pages 37–46, 2008.

[51] M. Kozanek, S. Wang, P. G. Passias, Q. Xia, G. Li, C. M. Bono, K. Wood, and G. Li. Range of motion and orientation of the lumbar facet joints in vivo. *Spine*, 34(19):E689–E696, 2009.

[52] J. M. Lambrecht, M. L. Audu, R. J. Triolo, and R. F. Kirsch. Musculoskeletal model of trunk and hips for development of seated-posture-control neuroprosthesis. *The Journal of Rehabilitation Research and Development*, 46(4):515–528, Jan 2009.

[53] W.-E. Lee, H.-W. Uhm, and Y.-S. Nam. Estimation of tendon slack length of knee extension/flexion muscle. *International Conference on Control, Automation and Systems*, pages 1–4, 2008.

[54] G. Li, S. Wang, P. Passias, Q. Xia, G. Li, and K. Wood. Segmental in vivo vertebral motion during functional human lumbar spine activities. *European Spine Journal*, 18(7):1013–1021, 2009.

[55] G. Lichtwark and A. Wilson. Optimal muscle fascicle length and tendon stiffness for maximising gastrocnemius efficiency during human walking and running. *Journal of Theoretical Biology*, 252(4):662–673, 2008.

[56] M. E. Lonnemann, S. V. Paris, and G. C. Gorniak. A morphological comparison of the human lumbar multifidus by chemical dissection. *Journal of Manual and Manipulative Therapy*, 16(4):E84–E92, 2008.

[57] R. M. Lumsden and J. M. Morris. An in vivo study of axial rotation and immobilization at the lumbosacral joint. *The Journal of Bone and Joint Surgery*, 50(8):1591, 1968.

[58] X. Luo and R. Pietrobon. Estimates and patterns of direct health care expenditures among individuals with back pain in the united states. *Spine*, 29(1):79, 2004.

[59] J. E. Macintosh and N. Bogduk. The biomechanics of the lumbar multifidus. *Clinical Biomechanics*, 1:205–213, 1986.

[60] J. E. Macintosh and N. Bogduk. The morphology of the human lumbar multifidus. *Spine*, 12(7):196–204, 1986.

[61] J. E. Macintosh and N. Bogduk. 1987 Volvo award in basic science. the morphology of the lumbar erector spinae. *Spine*, 12(7):658, 1987.

[62] J. E. Macintosh and N. Bogduk. The attachments of the lumbar erector spinae. *Spine*, 16(7):783–792, 1991.

[63] K. Manal and T. Buchanan. Subject-specific estimates of tendon slack length: A numerical method. *Journal of Applied Biomechanics*, 20:195–203, 2004.

[64] W. Marras, M. Jorgensen, K. P. Granata, and B. Wiand. Female and male trunk geometry: Size and prediction of the spine loading trunk muscles derived from MRI. *Clinical Biomechanics*, 16(1):38–46, 2001.

[65] B. Martin, R. Deyo, S. Mirza, J. Turner, B. Comstock, W. Hollingworth, and S. Sullivan. Expenditures and health status among adults with back and neck problems. *JAMA*, 299(6):656–664, 2008.

[66] S. McGill. A revised anatomical model of the abdominal musculature for torso flexion efforts. *Journal of Biomechanics*, 29(7):973–977, 1996.

[67] S. McGill, A. Childs, and C. Liebenson. Endurance times for low back stabilization exercises: Clinical targets for testing and training from a normal database. *Archives of Physical Medicine and Rehabilitation*, 80(8):941–944, 1999.

[68] S. McGill, R. Hughson, and K. Parks. Changes in lumbar lordosis modify the role of the extensor muscles. *Clinical Biomechanics*, 15(10):777–780, 2000.

[69] S. McGill, D. Juker, and P. Kropf. Appropriately placed surface EMG electrodes reflect deep muscle activity (psoas, quadratus lumborum, abdominal wall) in the lumbar spine. *Journal of Biomechanics*, 29(11):1503–1507, 1996.

[70] S. McGill, D. Juker, and P. Kropf. Quantitative intramuscular myoelectric activity of quadratus lumborum during a wide variety of tasks. *Clinical Biomechanics*, 11(3):170–172, 1996.

[71] S. McGill and R. Norman. Effects of an anatomically detailed erector spinae model on L4/L5 disc compression and shear. *Journal of Biomechanics*, 20(6):591–600, 1987.

[72] S. McGill and R. Norman. Potential of lumbodorsal fascia forces to generate back extension moments during squat lifts. *Journal of Biomedical Engineering*, 10(4):312–318, 1988.

[73] J. Meakin, J. Gregory, F. Smith, F. Gilbert, and R. Aspden. Characterizing the shape of the lumbar spine using an active shape model: Reliability and precision of the method. *Spine*, 33(7):807–813, 2008.

[74] J. R. Meakin, J. S. Gregory, R. M. Aspden, F. W. Smith, and F. J. Gilbert. The intrinsic shape of the human lumbar spine in the supine, standing and sitting postures: characterization using an active shape model. *Journal of Anatomy*, 215:206–211, 2009.

[75] W. Murray, T. Buchanan, and S. L. Delp. The isometric functional capacity of muscles that cross the elbow. *Journal of Biomechanics*, 33(8):943–952, 2000.

[76] A. Nachemson. Electromyographic studies on the vertebral portion of the psoas muscle: With special reference to its stabilizing function of the lumbar spine. *Acta Orthopaedica*, 37(2):177–190, 1966.

[77] A. Nachemson. The possible importance of the psoas muscle for stabilization of the lumbar spine. *Acta Orthopaedica*, 39(1-3):47–57, 1968.

[78] M. Nissan and I. Gilad. Dimensions of human lumbar vertebrae in the sagittal plane. *Journal of Biomechanics*, 19(9):753–8, 1986.

[79] R. S. Ochia, N. Inoue, S. M. Renner, E. P. Lorenz, T.-H. Lim, G. B. J. Andersson, and H. S. An. Three-dimensional in vivo measurement of lumbar spine segmental motion. *Spine*, 31(18):2073–8, 2006.

[80] O. M. O'Reilly, M. F. Metzger, J. M. Buckley, D. A. Moody, and J. C. Lotz. On the stiffness matrix of the intervertebral joint: Application to total disk replacement. *Journal of Biomechanical Engineering*, 131(8):081007, 2009.

[81] M. M. Panjabi. Centers and angles of rotation of body joints: a study of errors and optimization. *Journal of Biomechanics*, 12(12):911–920, 1979.

[82] M. M. Panjabi, R. A. Brand, and I. Augustus A White. Three-dimensional flexibility and stiffness properties of the human thoracic spine. *Journal of Biomechanics*, 9(4):185–192, 1976.

[83] M. M. Panjabi, V. K. Goel, T. Oxland, K. Takata, J. Duranceau, M. Krag, and M. Price. Human lumbar vertebrae: Quantitative three-dimensional anatomy. *Spine*, 17(3):299–306, 1992.

[84] M. J. Pearcy and N. Bogduk. Instantaneous axes of rotation of the lumbar intervertebral joints. *Spine*, 13(9):1033–41, 1988.

[85] M. J. Pearcy and S. Tibrewal. Axial rotation and lateral bending in the normal lumbar spine measured by three-dimensional radiography. *Spine*, 9(6):582–587, 1984.

[86] D. J. Pearsall, J. Reid, and L. Livingston. Segmental inertial parameters of the human trunk as determined from computed tomography. *Annals of Biomedical Engineering*, 24(2):198–210, 1996.

[87] D. J. Pearsall, J. Reid, and R. Ross. Inertial properties of the human trunk of males determined from magnetic resonance imaging. *Annals of Biomedical Engineering*, 22(6):692–706, 1994.

[88] S. Phillips, S. Mercer, and N. Bogduk. Anatomy and biomechanics of quadratus lumborum. *Proceedings of the Institution of Mechanical Engineers, Part H: Journal of Engineering in Medicine*, 222(2):151–159, 2008.

[89] A. Rosatelli, K. Ravichandiran, and A. Agur. Three-dimensional study of the musculotendinous architecture of lumbar multifidus and its functional implications. *Clinical Anatomy*, 21(6):539–546, 2008.

[90] P. Roussouly, S. Gollogly, E. Berthonnaud, and J. Dimnet. Classification of the normal variation in the sagittal alignment of the human lumbar spine and pelvis in the standing position. *Spine*, 30(3):346–353, 2005.

[91] A. Rozumalski, M. H. Schwartz, R. Wervey, A. Swanson, D. C. Dykes, and T. Novacheck. The in vivo three-dimensional motion of the human lumbar spine during gait. *Gait & Posture*, 28(3):378–84, 2008.

[92] P. Santaguida and S. McGill. The psoas major muscle: a three-dimensional geometric study. *Journal of Biomechanics*, 28(3):339–345, 1995.

[93] A. B. Schultz and G. B. J. Andersson. Analysis of loads on the lumbar spine. *Spine*, 6(1):76–82, 1981.

[94] C. Schwieters and G. Clore. Internal coordinates for molecular dynamics and minimization in structure determination and refinement. *Journal of Magnetic Resonance*, 152(2):288–302, 2001.

[95] A. Shirazi-Adl. Finite-element evaluation of contact loads on facets of an L2-L3 lumbar segment in complex loads. *Spine*, 16(5):533–541, 1991.

[96] I. A. F. Stokes and M. G. Gardner-Morse. Lumbar spine maximum efforts and muscle recruitment patterns predicted by a model with multijoint muscles and joints with stiffness. *Journal of Biomechanics*, 28(2):173–186, 1995.

[97] I. A. F. Stokes and M. G. Gardner-Morse. Quantitative anatomy of the lumbar musculature. *Journal of Biomechanics*, 32(3):311–316, 1999.

[98] I. A. F. Stokes, M. G. Gardner-Morse, D. Churchill, and J. P. Laible. Measurement of a spinal motion segment stiffness matrix. *Journal of Biomechanics*, 35(4):517–521, 2002.

[99] D. G. Thelen. Adjustment of muscle mechanics model parameters to simulate dynamic contractions in older adults. *Journal of Biomechanical Engineering*, 125:70–77, 2003.

[100] D. G. Thelen and F. C. Anderson. Using computed muscle control to generate forward dynamic simulations of human walking from experimental data. *Journal of Biomechanics*, 39(6):1107–1115, 2006.

[101] D. G. Thelen, F. C. Anderson, and S. L. Delp. Generating dynamic simulations of movement using computed muscle control. *Journal of Biomechanics*, 36(3):321–328, 2003.

[102] M. Troke, A. P. Moore, F. J. Maillardet, A. Hough, and E. Cheek. A new, comprehensive normative database of lumbar spine ranges of motion. *Clinical rehabilitation*, 15(4):371–379, 2001.

[103] J. van Dieën and I. Kingma. Total trunk muscle force and spinal compression are

lower in asymmetric moments as compared to pure extension moments. *Journal of Biomechanics*, 32(7):681–687, 1999.

[104] A. N. Vasavada, S. Li, and S. L. Delp. Influence of muscle morphometry and moment arms on the moment-generating capacity of human neck muscles. *Spine*, 23(4):412–422, 1998.

[105] S. M. Walker and G. Schrodt. I segment lengths and thin filament periods in skeletal muscle fibers of the rhesus monkey and the human. *Anat Rec*, 178(1):63–81, Jan 1974.

[106] S. Wang, P. Passias, G. Li, G. Li, and K. Wood. Measurement of vertebral kinematics using noninvasive image matching method-validation and application. *Spine*, 33(11):E355–E361, May 2008.

[107] S. R. Ward, C. M. Eng, L. H. Smallwood, and R. L. Lieber. Are current measurements of lower extremity muscle architecture accurate? *Clinical Orthopaedics and Related Research*, 467(4):1074–1082, 2009.

[108] S. R. Ward, C. W. Kim, C. M. Eng, L. J. Gottschalk, A. Tomiya, S. R. Garfin, and R. L. Lieber. Architectural analysis and intraoperative measurements demonstrate the unique design of the multifidus muscle for lumbar spine stability. *The Journal of Bone and Joint Surgery*, 91(1):176–185, 2009.

[109] S. R. Ward, A. Tomiya, G. J. Regev, B. E. Thacker, R. C. Benzl, C. W. Kim, and R. L. Lieber. Passive mechanical properties of the lumbar multifidus muscle support its role as a stabilizer. *Journal of Biomechanics*, 42(10):1384–1389, 2009.

[110] T. Weis-Fogh and M. N. Alexander. Scale effects in animal locomotion. *The Sustained Power Output From Striated Muscle.*, pages 511–525, 1977.

[111] A. A. White and M. M. Panjabi. *Clinical Biomechanics of the Spine.* Lippincott, Philadelphia :, 1978.

[112] A. Wilkenfeld, M. Audu, and R. J. Triolo. Feasibility of functional electrical stimulation for control of seated posture after spinal cord injury: A simulation study. *Journal of Rehabilitation Research and Development*, 43(2):139–152, 2006.

[113] H. J. Woltring, R. Huiskes, A. de Lange, and F. E. Veldpaus. Finite centroid and helical axis estimation from noisy landmark measurements in the study of human joint kinematics. *Journal of Biomechanics*, 18(5):379–389, 1985.

[114] K. Wong, K. Luk, J. Leong, S. Wong, and K. Wong. Continuous dynamic spinal motion analysis. *Spine*, 31(4):414–419, 2006.

[115] I. Yamamoto, M. M. Panjabi, T. Crisco, and T. Oxland. Three-dimensional movements of the whole lumbar spine and lumbosacral joint. *Spine*, 14(11):1256–1260, 1989.

[116] F. E. Zajac. Muscle and tendon: Properties, models, scaling, and application to biomechanics and motor control. *Critical Reviews in Biomedical Engineering*, 17(4):359–411, 1989.

Appendix A

Muscle Architecture Data

Table A.1: Quick guide to muscle parameters and terms

Length Terms		Force Terms		Constants and Subscripts	
ℓ^{MT}	Musculotendon Length	F^M	Muscle force	k	stiffness or shape factor
ℓ^M	Muscle Length	F_O^M	Maximum isometric force	$[\quad]_{toe}$	transition region
ℓ_O^M	Optimal fiber length	f_l	Normalized muscle force	$[\quad]_{lin}$	at linear region
$\bar{L}^M$	Normalized muscle length	F^T	Tendon Force	PE	passive element
ℓ^T	Tendon length	$\bar{F}^T$	Normalized tendon force	CE	contractile element
ℓ_S^T	Tendon slack length			γ	Gaussian shape factor
ℓ^S	Sarcomere length			K	Specific Tension (N/cm^2)
ε^T	Tendon strain			$[\quad]_0$	at maximum force
ε^M	Passive muscle strain			α	pennation angle

Table A.2: Muscle modeling parameters: PCSA mm^2, maximum isometric force F_o^M (N), a ratio of the muscle fiber length to the musculotendon length ℓ^f/ℓ^{MT}, sarcomere length $\ell^S(\mu m)$, optimal fiber length ℓ_o^M (m), pennation angle α (degrees), and tendon slack length ℓ_S^T (m). The source of this data is given at the top of each muscle column. Note: *via* implies this data was not explicitly given, but it was determined graphically or by description.

Muscle Group	Name	PCSA	F_o^M	ℓ^f/ℓ^{MT}	ℓ^S	ℓ_o^M	α	ℓ_S^T
Psoas Major		[15]		*est.* [38]	[107]		[8]	
	Ps_L1_VB	211	97	0.800	3.11	0.1841	10.7	0.0647
	Ps_L1_TP	61	28	0.800	3.11	0.1818	10.7	0.0639
	Ps_L2_TP	211	97	0.800	3.11	0.1597	10.7	0.0561
	Ps_L3_TP	101	46	0.800	3.11	0.1394	10.7	0.0490
	Ps_L4_TP	161	74	0.800	3.11	0.1195	10.7	0.0420
	Ps_L5_TP	173	80	0.800	3.11	0.1034	10.7	0.0363
	Ps_L5_VB	191	88	0.800	3.11	0.0903	10.7	0.0317
	Ps_L1_L2_IVD	120	55	0.800	3.11	0.1660	10.7	0.0583
	Ps_L2_L3_IVD	119	55	0.800	3.11	0.1440	10.7	0.0506
	Ps_L3_L4_IVD	36	17	0.800	3.11	0.1235	10.7	0.0434
	Ps_L4_L5_IVD	79	36	0.800	3.11	0.0998	10.7	0.0351
Rectus Abdominis		[97]		[25]	[25]		[25]	
	rect_abd	567	261	0.788	2.83	0.2986	0	0.0810
Erector Spinae		[14]		[25]	[25]		[25]	
Iliocostalis Lumborum	IL_L4	189	87	0.274	2.37	0.0167	13.8	0.0354
pars Lumborum	IL_L3	182	84	0.274	2.37	0.0252	13.8	0.0533
	IL_L2	154	71	0.274	2.37	0.0373	13.8	0.0789
	IL_L1	108	50	0.274	2.37	0.0514	13.8	0.1089
Iliocostalis Lumborum	IL_r5	23	11	0.381	2.37	0.1546	13.8	0.2165
pars Thoracis	IL_r6	31	14	0.417	2.37	0.1483	13.8	0.1793
	IL_r7	39	18	0.452	2.37	0.1459	13.8	0.1536
	IL_r8	34	16	0.462	2.37	0.1293	13.8	0.1308
	IL_r9	50	23	0.600	2.37	0.1424	13.8	0.0838
	IL_r10	100	46	0.600	2.37	0.1175	13.8	0.0692
	IL_r11	123	57	0.640	2.37	0.1011	13.8	0.0506
	IL_r12	147	68	0.640	2.37	0.0731	13.8	0.0366
Longissimus Thoracis	LTpT_t1	29	13	0.260	2.31	0.1028	12.6	0.2430
pars Thoracis	LTpT_t2	57	26	0.257	2.31	0.1061	12.6	0.2550
	LTpT_t3	56	26	0.257	2.31	0.1067	12.6	0.2565
	LTpT_t4	23	10	0.257	2.31	0.1068	12.6	0.2566
	LTpT_t5	22	10	0.257	2.31	0.1008	12.6	0.2421
	LTpT_t6	32	15	0.267	2.31	0.1031	12.6	0.2360
Continued on next page								

Muscle Group	Name	PCSA	F_o^M	ℓ^f/ℓ^{MT}	ℓ^S	ℓ_o^M	α	ℓ_S^T
	LTpT_t7	39	18	0.306	2.31	0.1183	12.6	0.2236
	LTpT_t8	63	29	0.346	2.31	0.1261	12.6	0.1997
	LTpT_t9	73	34	0.330	2.31	0.1244	12.6	0.2108
	LTpT_t10	80	37	0.330	2.31	0.1123	12.6	0.1903
	LTpT_t11	84	38	0.330	2.31	0.0962	12.6	0.1631
	LTpT_t12	69	32	0.330	2.31	0.0753	12.6	0.1275
	LTpT_r4	23	10	0.330	2.31	0.1358	12.6	0.2302
	LTpT_r5	22	10	0.330	2.31	0.1273	12.6	0.2157
	LTpT_r6	32	15	0.353	2.31	0.1348	12.6	0.2065
	LTpT_r7	39	18	0.333	2.31	0.1284	12.6	0.2144
	LTpT_r8	63	29	0.290	2.31	0.1051	12.6	0.2145
	LTpT_r9	73	34	0.254	2.31	0.0909	12.6	0.2222
	LTpT_r10	80	37	0.327	2.31	0.1059	12.6	0.1817
	LTpT_r11	84	38	0.370	2.31	0.1013	12.6	0.1445
	LTpT_r12	69	32	0.300	2.31	0.0633	12.6	0.1230
Longissimus Thoracis	LTpL_L1	79	36	0.419	2.31	0.0811	12.6	0.0944
pars Lumborum	LTpL_L2	91	42	0.433	2.31	0.0677	12.6	0.0744
	LTpL_L3	103	47	0.436	2.31	0.0549	12.6	0.0596
	LTpL_L4	110	51	0.438	2.31	0.0392	12.6	0.0424
	LTpL_L5	116	53	1.000	2.31	0.0504	12.6	0.0019
Quadratus Lumborum		[88]		[25]	[25]		[25]	
	QL_post_I.1-L3	40	18	0.505	2.38	0.0384	7.4	0.0322
	QL_post_I.2-L4	53	24	0.505	2.38	0.0222	7.4	0.0186
	QL_post_I.2-L3	31	14	0.505	2.38	0.0502	7.4	0.0421
	QL_post_I.2-L2	19	9	0.505	2.38	0.0348	7.4	0.0292
	QL_post_I.3-L1	28	13	0.624	2.38	0.0856	7.4	0.0445
	QL_post_I.3-L2	30	14	0.505	2.38	0.0504	7.4	0.0423
	QL_post_I.3-L3	50	23	0.505	2.38	0.0361	7.4	0.0303
	QL_mid_L3-12.3	13	6	0.624	2.38	0.0546	7.4	0.0284
	QL_mid_L3-12.2	14	7	0.624	2.38	0.0579	7.4	0.0301
	QL_mid_L3-12.1	24	11	0.624	2.38	0.0631	7.4	0.0328
	QL_mid_L2-12.1	20	9	0.624	2.38	0.0408	7.4	0.0212
	QL_mid_L4-12.3	12	5	0.624	2.38	0.0729	7.4	0.0379
	QL_ant_I.2-T12	15	7	0.624	2.38	0.1045	7.4	0.0543
	QL_ant_I.3-T12	29	7	0.624	2.38	0.1033	7.4	0.0537
	QL_ant_I.2-12.1	10	5	0.624	2.38	0.0999	7.4	0.0519
	QL_ant_I.3-12.1	19	9	0.624	2.38	0.0987	7.4	0.0512
	QL_ant_I.3-12.2	13	6	0.624	2.38	0.0929	7.4	0.0482
	QL_ant_I.3-12.3	15	7	0.624	2.38	0.0869	7.4	0.0451
Multifidus		[14]		[89]	[108]		[4]	
	MF_m1s	40	18	0.661	2.27	0.0468	0	0.0195
	MF_m1t.1	42	19	0.730	2.27	0.0752	0	0.0225
	MF_m1t.2	36	17	0.730	2.27	0.0943	0	0.0283

Muscle Group	Name	PCSA	F_o^M	ℓ^f/ℓ^{MT}	ℓ^S	ℓ_o^M	α	ℓ_S^T
	MF_m1t.3	60	28	0.730	2.27	0.1030	0	0.0309
	MF_m2s	39	18	0.677	2.27	0.0454	0	0.0176
	MF_m2t.1	39	18	0.727	2.27	0.0639	0	0.0194
	MF_m2t.2	99	46	0.727	2.27	0.0809	0	0.0246
	MF_m2t.3	99	46	0.727	2.27	0.0917	0	0.0279
	MF_m3s	54	25	0.661	2.27	0.0397	0	0.0165
	MF_m3t.1	52	24	0.709	2.27	0.1028	0	0.0342
	MF_m3t.2	52	24	0.709	2.27	0.0854	0	0.0284
	MF_m3t.3	52	24	0.709	2.27	0.0854	0	0.0284
	MF_m4s	47	21	0.562	2.27	0.0372	0	0.0235
	MF_m4t.1	47	21	0.667	2.27	0.0548	0	0.0222
	MF_m4t.2	47	21	0.667	2.27	0.0734	0	0.0297
	MF_m4t.3	47	21	0.667	2.27	0.0848	0	0.0344
	MF_m5s	23	10	0.562	2.27	0.0147	0	0.0093
	MF_m5t.1	23	10	0.667	2.27	0.0759	0	0.0308
	MF_m5t.2	23	10	0.667	2.27	0.0568	0	0.0230
	MF_m5t.3	23	10	0.667	2.27	0.0175	0	0.0071
	MF_m1.laminar	19	9	0.681	2.27	0.0313	0	0.0119
	MF_m2.laminar	22	10	0.681	2.27	0.0269	0	0.0102
	MF_m3.laminar	23	11	0.681	2.27	0.0262	0	0.0099
	MF_m4.laminar	17	8	0.681	2.27	0.0286	0	0.0109
	MF_m5.laminar	36	17	0.681	2.27	0.0256	0	0.0097
External Oblique		[97]		*est.* [38]	[25]		[25]	
	EO1	196	90	0.389	2.83	0.0359	0	0.0570
	EO2	232	107	0.410	2.83	0.0379	0	0.0552
	EO3	243	112	0.455	2.83	0.0384	0	0.0466
	EO4	234	108	0.470	2.83	0.0393	0	0.0448
	EO5	273	126	0.480	2.83	0.0471	0	0.0515
	EO6	397	183	0.500	2.83	0.0565	0	0.0571
Internal Oblique		[97]		*est.* [38]	[25]		[25]	
	IO1	185	85	0.400	2.83	0.0422	0	0.0640
	IO2	224	103	0.400	2.83	0.0435	0	0.0659
	IO3	226	104	0.400	2.83	0.0517	0	0.0783
	IO4	268	123	0.600	2.83	0.0697	0	0.0470
	IO5	235	108	0.600	2.83	0.0568	0	0.0383
	IO6	207	95	0.600	2.83	0.0544	0	0.0367
Latissimus Dorsi		[13]		*est.* [13]				
	LD_L1	90	41	0.790	2.3	0.3161	0	0.0692
	LD_L2	90	41	0.790	2.3	0.3383	0	0.0741
	LD_L3	110	51	0.790	2.3	0.3551	0	0.0778
	LD_L4	110	51	0.790	2.3	0.3719	0	0.0815
	LD_L5	110	51	0.800	2.3	0.3902	0	0.0801
	LD_T7	40	18	0.800	2.3	0.2238	0	0.0460

Muscle Group	Name	PCSA	F_o^M	ℓ^f/ℓ^{MT}	ℓ^S	ℓ_o^M	α	ℓ_S^T
	LD_T8	40	18	0.800	2.3	0.2325	0	0.0477
	LD_T9	40	18	0.840	2.3	0.2570	0	0.0402
	LD_T10	60	28	0.840	2.3	0.2797	0	0.0438
	LD_T11	60	28	0.800	2.3	0.2848	0	0.0585
	LD_T12	50	23	0.800	2.3	0.3032	0	0.0623
	LD_R11	60	28	0.800	2.3	0.2407	0	0.0494
	LD_R12	40	18	0.800	2.3	0.2445	0	0.0502
	LD_Il	70	32	0.950	2.3	0.4321	0	0.0187